

# Wave instabilities in anisotropic regularized Kappa plasmas: New plasma dispersion functions and numerical validation

Rudi Gaelzer,<sup>1</sup> Dustin L. Schröder,<sup>2</sup> Marian Lazar,<sup>2,3</sup> and Horst Fichtner<sup>2</sup>

<sup>1</sup>*Instituto de Física, Universidade Federal do Rio Grande do Sul, CP 15051, 91501-970, Porto Alegre, RS, Brazil*

<sup>2</sup>*Institut für Theoretische Physik IV, Ruhr-Universität Bochum, Universitätsstrasse 150, 44780 Bochum, Germany*

<sup>3</sup>*Centre for Mathematical Plasma Astrophysics, Department of Mathematics, KU Leuven, Belgium*

(\*Electronic mail: [rudi.gaelzer@ufrgs.br](mailto:rudi.gaelzer@ufrgs.br))

Plasmas in space and astrophysical environments are frequently found in (quasi-)stationary states not in thermal equilibrium, indicated by velocity distribution functions (VDFs) featuring nonthermal characteristics, such as Lorentzian high-energy tails and kinetic (temperature and strahl/beam) anisotropies. For decades, in-situ observations of electrons and ions in the solar corona, solar wind or planetary magnetospheres have been modelled using so-called Kappa VDFs, whose standard form, however - depending on the considered VDF moment - imposes stringent constraints on the minimum value of the Kappa power-law parameter. Such limitations have posed difficulties on the derivation of a fully-consistent hydrodynamic formulation of suprathermal plasmas. To improve this situation, the recently proposed regularized Kappa VDF avoids strict constraints on the Kappa parameter by introducing an exponential, regularizing cut-off. In this work we assume that the plasma particles are described by regularized-Kappa VDFs that feature anisotropies not only in their thermal velocity spread parameters but also in their exponential cut-offs. The dielectric tensor components for waves propagating along a magnetic field are derived, in terms of new plasma dispersion functions. The resulting dispersion equations are solved with two complementary techniques, namely by using the analytical expressions derived here and by employing the ALPS code. This is done for physical parameters that give rise to electromagnetic and electrostatic instabilities. Both approaches show excellent agreement and the results demonstrate how an anisotropy in the regularizing cut-off of VDFs can serve, depending on an instability's nature, either as a stabilization factor or as an additional free energy source.

Keywords: Kappa plasmas, Regularized Kappa distribution, Kinetic theory of plasmas, Waves in magnetized plasmas.

## I. INTRODUCTION

Space plasmas are typically hot and dilute, and therefore nearly collisionless. As a result, these plasmas are not in thermodynamic equilibrium, which in-situ observations attribute primarily to kinetic anisotropies and suprathermal populations<sup>1-3</sup>. Interest for understanding such observational evidences and their impact in the solar wind and planetary environments is currently extending to the solar corona, driven by ongoing exploration through the Parker Solar Probe<sup>4,5</sup> and Solar Orbiter missions<sup>6,7</sup>. It is expected that the dynamics and properties of such weakly collisional plasmas are governed by wave fluctuations, including the kinetic instabilities induced by the anisotropies of the velocity distributions<sup>8</sup>. These instabilities can be stimulated by the suprathermal populations<sup>9,10</sup>, and the resulting plasma fluctuations interact back with the particles, limiting their anisotropies<sup>1,11</sup>.

Despite such nonlinear coupling of the plasma fluctuations with the plasma populations, linear dispersion theory remains to be a valuable standard tool<sup>12,13</sup> for the studies of plasma instabilities because predictions from linear theory are essential for interpreting observations<sup>1,14</sup>, for calibrating numerical simulations<sup>15</sup>, and for developing extended quasi-linear theories<sup>13,14</sup>. This involves determining the nature of the waves, frequency ranges, and unstable wave numbers, as well as identifying the fastest-growing modes expected to drive the resulting enhanced waves and the relaxation of anisotropies.

Realistic predictions require velocity distribution functions (VDFs) that closely reproduce in-situ observations. Thus, the observed VDFs of plasma populations (electrons and protons/ions) reveal not only temperature anisotropies and beam (or drifting) populations, but also suprathermal tails at high energies. This led to the introduction of so-called Kappa VDFs<sup>16-18</sup> and their anisotropic forms<sup>19-21</sup> as upgrades to idealized Maxwellian models, capable of capturing both the quasi-thermal core at low energies and the suprathermal tails; for recent advancements in these models see Ref. 22.

Despite these efforts, the results may be affected by flaws in empirical Kappa models, such as the restriction in defining the moments and in the hydrodynamic macro-modeling<sup>23</sup> to sufficiently high values of the parameter  $\kappa$ , or the undesired non-physical effects of superluminal particles with speeds higher than the speed of light unavoidably occurring in a non-relativistic model<sup>24</sup>. To overcome these and other shortcomings, isotropic<sup>18</sup> and anisotropic<sup>20</sup> regularized Kappa distributions (RKDs) have been proposed, which in addition to a power-law part exhibit an exponential (Maxwellian-like) cut-off to limit an unrealistic extent of suprathermal tails. Adding such cut-off significantly complicates the analysis, making it harder to analytically derive the dielectric properties essential for studying waves and instabilities. Nonetheless, RKDs are gaining ground in many applications<sup>21,25-28</sup>, also motivating advances in the analysis of wave dispersion properties with numerical and even theoretical tools<sup>29-33</sup>.

However, the anisotropic RKDs were, so far, mostly em-

ployed under the assumption of an isotropic cut-off, i.e. a common regularization parameter of the distribution function along and perpendicular to the magnetic field. Given that this does not exploit the full flexibility to model an anisotropy of an RKD, this is referred to as the *semi-anisotropic* case.

In the present work, we address the more general case of a *fully anisotropic* RKD, which, in addition to anisotropic 'thermal' speeds, also takes into account different cut-off parameters in the principal directions, parallel ( $\parallel$ ) and perpendicular ( $\perp$ ) to the magnetic field, so that the temperature anisotropy is also determined by such anisotropic cut-off. Such fully anisotropic RKD has only been considered in a numerical analysis of electromagnetic instabilities<sup>29</sup>. In fact, most of the existing dispersion and stability analyses of RKD plasmas rely on numerical solvers<sup>29,32,33</sup> due to the lack of adequate analytical expressions, such as the plasma dispersion functions, i.e., integral functions and, implicitly, the dielectric tensor components specific to RKD plasmas. However, ensuring the reliability of numerical solvers demands extensive validation across both standard and non-standard distributions and their analytical result<sup>34-37</sup>.

Motivated by these needs, in the present paper we extend the semi-analytical approach by deriving dispersion functions for fully anisotropic RKD plasmas. This way, we provide a most flexible and general tool for the analysis of kinetic instabilities and, at the same time, useful test cases for the validation of fully numerical approaches.

The paper is organized as follows. In section II the dispersion theory based on a fully anisotropic RKD is worked out analytically by deriving anisotropic dispersion functions, and these are implemented in the components of susceptibility tensor for parallel propagation. Then, sections III and IV contain the applications describing electromagnetic instabilities driven by anisotropic electrons with semi- and fully anisotropic RKDs. Finally, a summary of the results and the primary conclusions are presented in section V.

## II. THEORETICAL FORMULATION

In this section, the basic formalism employed in our work will be introduced.

### A. The generalized anisotropic RKD with drift

The model VDF to be employed in this work extends both the generalized form introduced by Refs. 20 and 30, and the drift-anisotropic distribution employed by Ref. 33, namely

$$f_{\kappa, \boldsymbol{\theta}}^{(\eta, \zeta, \boldsymbol{\mu})}(v_{\parallel}, v_{\perp}) = N_{\kappa, \boldsymbol{\theta}}^{(\eta, \zeta, \boldsymbol{\mu})} \left[ 1 + \frac{(v_{\parallel} - U_{\parallel})^2}{\eta \theta_{\parallel}^2} + \frac{v_{\perp}^2}{\eta \theta_{\perp}^2} \right]^{-\zeta} \times \exp \left[ -\frac{\mu_{\parallel}}{\theta_{\parallel}^2} (v_{\parallel} - U_{\parallel})^2 - \frac{\mu_{\perp}}{\theta_{\perp}^2} v_{\perp}^2 \right], \quad (1)$$

where  $\boldsymbol{\theta} = (\theta_{\parallel}, \theta_{\perp})$ ,  $\boldsymbol{\mu} = (\mu_{\parallel}, \mu_{\perp})$  and  $N_{\kappa, \boldsymbol{\theta}}^{(\eta, \zeta, \boldsymbol{\mu})}$  is the normalization constant. In (1), parameters  $\eta$  and  $\zeta$  are coupled

via  $\kappa$  parameter, as in the standard Kappa VDFs recovered for  $\mu_{\parallel} = \mu_{\perp} = 0$ , with  $\eta = \kappa$  and  $\zeta = \kappa + 1$ . Instead,  $\mu_{\parallel, \perp}$  are typical dimensionless constants<sup>21,29</sup> that do not necessarily depend on  $\kappa$ . Their values balance the reduction of unphysical effects of superluminal particles with the need to retain suprathermal populations in the high-energy tails<sup>24</sup>. As it will be shown below, the normalization parameters  $\theta_{\parallel, \perp}$  directly link to the temperature components  $T_{\kappa, \parallel, \perp}$  (in energy units), as for (drifting) standard bi-Kappa VDFs<sup>30,34,35</sup>.

$$T_{\kappa, \parallel, \perp} = \frac{\kappa}{\kappa - 3/2} \frac{m \theta_{\parallel, \perp}^2}{2}, \quad (2)$$

with  $m$  the particle mass. In this case, the limit  $\kappa \rightarrow \infty$  will restore the drifting bi-Maxwellian (dbM) VDF

$$f_{\text{dbM}}(v_{\parallel}, v_{\perp}) = \frac{1}{\pi^{3/2} \theta_{\parallel} \theta_{\perp}^2} \exp \left( -\frac{(v_{\parallel} - U_{\parallel})^2}{\theta_{\parallel}^2} - \frac{v_{\perp}^2}{\theta_{\perp}^2} \right), \quad (3)$$

with temperature components  $T_{M, \parallel, \perp} = m \theta_{\parallel, \perp}^2 / 2 < T_{\kappa, \parallel, \perp}$ <sup>22,38</sup>.

In the isotropic case  $\theta_{\parallel} = \theta_{\perp} = \theta$  and  $\mu_{\parallel} = \mu_{\perp} = \mu$ , distribution (1) reduces to the model employed by Ref. 30, whereas in the case  $\mu_{\parallel} = \mu_{\perp} = \alpha^2$  (with  $\theta_{\parallel} \neq \theta_{\perp}$ ), we obtain the anisotropic distribution adopted by Ref. 33. A further limiting case without the drift ( $U_{\parallel} = 0$ ) reproduces the anisotropic VDF adopted by Ref. 32. Our form (1), therefore, introduces further flexibility by allowing separate choices for the regularization parameters ( $\mu_{\parallel}, \mu_{\perp}$ ) in either direction.

We will now obtain an equivalent form for the generalized RKD, suitable for the ensuing evaluation of the dielectric tensor. This is accomplished via the identity

$$\int_0^{\infty} \beta^{-\delta} e^{-\gamma \beta} d\beta = \Gamma(1 - \delta) \gamma^{\delta-1} \quad (\gamma > 0),$$

which renders (1) as

$$f_{\kappa, \boldsymbol{\theta}}^{(\eta, \zeta, \boldsymbol{\mu})}(v_{\parallel}, v_{\perp}) = \frac{N_{\kappa, \boldsymbol{\theta}}^{(\eta, \zeta, \boldsymbol{\mu})}}{\Gamma(\zeta)} \times \int_0^{\infty} d\beta \beta^{\zeta-1} e^{-\beta} e^{-(v_{\parallel} - U_{\parallel})^2 / \theta_{\parallel}^2} e^{-v_{\perp}^2 / \theta_{\perp}^2}, \quad (4)$$

where

$$\phi_{\parallel, \perp}(\beta) = \frac{\theta_{\parallel, \perp}}{\sqrt{\mu_{\parallel, \perp} + \beta / \eta}}.$$

We will first use (4) to obtain the normalization constant  $N_{\kappa, \boldsymbol{\theta}}^{(\eta, \zeta, \boldsymbol{\mu})}$ , which is determined from the condition

$$\int d^3 v f_{\kappa, \boldsymbol{\theta}}^{(\eta, \zeta, \boldsymbol{\mu})}(v_{\parallel}, v_{\perp}) = 1.$$

Inserting (4), we can easily evaluate the velocity integrals using a cylindrical coordinate system, resulting in

$$\pi^{3/2} \theta_{\parallel} \theta_{\perp}^2 \frac{N_{\kappa, \boldsymbol{\theta}}^{(\eta, \zeta, \boldsymbol{\mu})}}{\Gamma(\zeta)} \int_0^{\infty} d\beta \frac{\beta^{\zeta-1} e^{-\beta}}{\sqrt{\mu_{\parallel} + \beta / \eta} (\mu_{\perp} + \beta / \eta)} = 1.$$

The remaining integral is identified with (A2a) and with the identity (A8), providing the final expression

$$N_{\kappa, \boldsymbol{\theta}}^{(\eta, \zeta, \boldsymbol{\mu})} = \left[ (\pi\eta)^{3/2} \theta_{\parallel} \theta_{\perp}^2 \mathcal{U}^{(\eta, \zeta, \boldsymbol{\mu})} \right]^{-1},$$

where  $\mathcal{U}^{(\eta, \zeta, \boldsymbol{\mu})} \equiv \mathcal{U}_{0,0}^{(\eta, \zeta, \boldsymbol{\mu})}$ , the latter being given by expressions (A7) and (A9). Notice that in the  $\mu$ -isotropic limit (*i.e.*,  $\mu_{\parallel} = \mu_{\perp} = \mu$ ), one obtains the known expressions<sup>20,30</sup>

$$\begin{aligned} \mathcal{U}^{(\eta, \zeta, \boldsymbol{\mu})} &= U\left(\frac{3}{2}, \frac{5}{2} - \zeta, \eta\boldsymbol{\mu}\right) \\ &= (\eta\boldsymbol{\mu})^{\zeta-3/2} U\left(\zeta, \zeta - \frac{1}{2}, \eta\boldsymbol{\mu}\right), \end{aligned}$$

where  $U(a, b, z)$  is the second solution of Kummer's equation, known as Tricomi function (see eq. A4).

Other important physical properties that can be derived from (4) are the perpendicular (parallel) kinetic temperatures, evaluated from the second moments of the VDF according to  $T_{\perp} = \frac{1}{2}m\langle v_{\perp}^2 \rangle$  and  $T_{\parallel} = m\langle (v_{\parallel} - U_{\parallel})^2 \rangle$ . Employing expressions (A2a) and (A8), one obtains

$$T_{\perp, \kappa, \boldsymbol{\theta}}^{(\eta, \zeta, \boldsymbol{\mu})} = \frac{1}{2}m\theta_{\perp}^2 \eta \frac{\mathcal{U}_{0,1}^{(\eta, \zeta, \boldsymbol{\mu})}}{\mathcal{U}_{0,0}^{(\eta, \zeta, \boldsymbol{\mu})}}, \quad T_{\parallel, \kappa, \boldsymbol{\theta}}^{(\eta, \zeta, \boldsymbol{\mu})} = \frac{1}{2}m\theta_{\parallel}^2 \eta \frac{\mathcal{U}_{1,0}^{(\eta, \zeta, \boldsymbol{\mu})}}{\mathcal{U}_{0,0}^{(\eta, \zeta, \boldsymbol{\mu})}}. \quad (5)$$

These results show that the temperatures of a fully-anisotropic RKD depend not only on the thermal velocity parameters  $\theta_{\perp(\parallel)}$  but also on the regularization parameters  $\mu_{\perp(\parallel)}$ , via the  $\mathcal{U}_{\alpha, \beta}^{(\eta, \zeta, \boldsymbol{\mu})}$  functions discussed in Appendix A. In fact, if  $\mu_{\perp} \neq \mu_{\parallel}$ , a higher degree of anisotropy is possible (compared to the Maxwellian and standard Kappa VDFs), in such a way that  $T_{\perp}/\theta_{\perp}^2 \neq T_{\parallel}/\theta_{\parallel}^2$ . The kinetic temperatures (2) for a standard bi-Kappa VDF are the limiting case of the results above when  $\mu_{\perp(\parallel)} \rightarrow 0$ , as one can verify after introducing the limit (A11) and taking the usual  $\eta = \kappa$  and  $\zeta = \kappa + 1$ .

## B. The dielectric tensor and the dispersion equations

We consider waves propagating parallel to the (homogeneous) magnetic field  $\mathbf{B}_0 = B_0 \hat{\mathbf{z}}$  ( $B_0 > 0$ ). In this case the only nonzero Cartesian components of the dielectric tensor are  $\varepsilon_{xx} = \varepsilon_{yy} = \varepsilon_1$ ,  $\varepsilon_{xy} = -\varepsilon_{yx} = \varepsilon_2$ , and  $\varepsilon_{zz} = \varepsilon_3$ , written as<sup>39</sup>

$$\varepsilon_i = \delta_{i1} + \delta_{i3} + \sum_a \chi_i^{(a)} \quad (i = 1, 2, 3),$$

where  $\chi_i^{(a)}$  is the  $i$ -th component of the susceptibility tensor associated with particle species/population  $a = (e, i, \dots)$ . For a gyrotropic distribution function  $f_{a0} = f_{a0}(v_{\parallel}, v_{\perp})$ , the susceptibility components for parallel propagation are<sup>39</sup>

$$\chi_1^{(a)} = \frac{1}{4} \frac{\omega_{pa}^2}{\omega^2} \sum_{s=\pm 1} \int d^3v \frac{v_{\perp} \mathcal{L} f_{a0}}{\omega - s\Omega_a - k_{\parallel} v_{\parallel}} \quad (6a)$$

$$\chi_2^{(a)} = i \frac{1}{4} \frac{\omega_{pa}^2}{\omega^2} \sum_{s=\pm 1} s \int d^3v \frac{v_{\perp} \mathcal{L} f_{a0}}{\omega - s\Omega_a - k_{\parallel} v_{\parallel}} \quad (6b)$$

$$\chi_3^{(a)} = \frac{\omega_{pa}^2}{k_{\parallel}} \int d^3v \frac{\partial f_{a0} / \partial v_{\parallel}}{\omega - k_{\parallel} v_{\parallel}}. \quad (6c)$$

In (6b) – (6c),  $v_{\parallel}$  and  $v_{\perp}$  are, respectively, the parallel and perpendicular (to  $\mathbf{B}_0$ ) components of the particle velocity. Likewise,  $k_{\parallel}$  is the parallel component of the wavevector ( $k_{\perp} = 0$ ) and  $\omega$  is the wave angular frequency. Each particle species/population is characterized by its number density  $n_a$  and the particle's mass  $m_a$  and charge  $q_a$ . Accordingly,  $\omega_{pa} = \sqrt{4\pi n_a q_a^2 / m_a}$  and  $\Omega_a = q_a B_0 / m_a c$  are the  $a$ -species plasma and cyclotron frequencies, with  $c$  being the vacuum light speed. Finally,

$$\mathcal{L} f_{a0} = (\omega - k_{\parallel} v_{\parallel}) \frac{\partial f_{a0}}{\partial v_{\perp}} + k_{\parallel} v_{\perp} \frac{\partial f_{a0}}{\partial v_{\parallel}}.$$

The linearized Vlasov-Maxwell equations leads to the wave equation for a magnetized plasma that, in the case of parallel propagation and in the Fourier  $(\mathbf{k}, \omega)$  space, factors into two branches:<sup>39</sup> the dispersion equation for longitudinal waves

$$\varepsilon_3 = 1 + \sum_a \chi_3^{(a)} = 0, \quad (7)$$

and the dispersion equations for electromagnetic waves

$$N_s^2 = 1 + \sum_a \left( \chi_1^{(a)} - s i \chi_2^{(a)} \right) \quad (s = \pm 1), \quad (8)$$

where  $N_s = k_{\parallel} c / \omega_s$  is the index of refraction of the  $s$ -th mode. For  $s = +1$  the equation describes left-handed circularly polarized ( $L$ ) waves ( $N_+ = N_L$ ), whereas the equation for  $s = -1$  corresponds to right-handed ( $R$ ) waves ( $N_- = N_R$ ). The dispersion equations (7) and (8) depend on the evaluation of the components (6a-c) of the susceptibility tensor for all plasma species/populations, and ultimately on the evaluation of the integrals contained therein.

The susceptibility tensor of a species described by the anisotropic drifting bi-RKD (hereafter identified by the shortened acronym “dbRK”) was obtained. The evaluation of the integrals is simplified if one employs the form (4) of the VDF, and the susceptibility tensor components can be written as

$$\chi_1^{(\text{dbRK})} = \frac{1}{2} \frac{\omega_{pa}^2}{\omega^2} \sum_{s=\pm 1} \left[ \zeta_0 Z_{\kappa}^{(\eta, \zeta, \boldsymbol{\mu})}(\zeta_s) + \frac{1}{2} \mathcal{Z}_{\kappa, \boldsymbol{\theta}}^{(\eta, \zeta, \boldsymbol{\mu})'}(\zeta_s) \right] \quad (9a)$$

$$\chi_2^{(\text{dbRK})} = \frac{i}{2} \frac{\omega_{pa}^2}{\omega^2} \sum_{s=\pm 1} s \left[ \zeta_0 Z_{\kappa}^{(\eta, \zeta, \boldsymbol{\mu})}(\zeta_s) + \frac{1}{2} \mathcal{Z}_{\kappa, \boldsymbol{\theta}}^{(\eta, \zeta, \boldsymbol{\mu})'}(\zeta_s) \right] \quad (9b)$$

$$\chi_3^{(\text{dbRK})} = -\frac{\omega_{pa}^2}{k_{\parallel}^2 \theta_{\parallel}^2} Z_{\kappa}^{(\eta, \zeta, \boldsymbol{\mu})'}(\zeta_0). \quad (9c)$$

The new dispersion functions  $Z_{\kappa}^{(\eta, \zeta, \boldsymbol{\mu})}(z)$  and  $\mathcal{Z}_{\kappa, \boldsymbol{\theta}}^{(\eta, \zeta, \boldsymbol{\mu})}(z)$ , as well as their derivatives  $Z_{\kappa}^{(\eta, \zeta, \boldsymbol{\mu})'} = dZ_{\kappa}^{(\eta, \zeta, \boldsymbol{\mu})}/dz$  and

$\mathcal{Z}_{\kappa, \theta}^{(\eta, \zeta, \mu)'} = d\mathcal{Z}_{\kappa, \theta}^{(\eta, \zeta, \mu)}/dz$ , are defined and analysed in section II C. Their arguments are ( $n = 0, \pm 1$ )

$$\zeta_n = \xi_n - \frac{U_{\parallel}}{\theta_{\parallel}}, \quad \xi_n = \frac{\omega - n\Omega}{k_{\parallel} \theta_{\parallel}}.$$

### C. The dispersion functions for anisotropic RKD plasmas

As oftentimes happens whenever one endeavours to devise an analytical description for the dispersive properties of waves propagating in (and interacting with) plasmas statistically described by new forms of VDFs, this objective can only be achieved by defining new dispersion functions. In this section two new functions (and their derivatives) are defined for dbRK VDFs, and some of their properties are derived.

Thus, the new dispersion function associated to longitudinal waves is

$$\begin{aligned} Z_{\kappa}^{(\eta, \zeta, \mu)}(z) &= \frac{\eta^{-3/2}}{\mathcal{U}(\eta, \zeta, \mu)} \frac{1}{\Gamma(\zeta)} \\ &\times \int_0^{\infty} d\beta \frac{\beta^{\zeta-1} e^{-\beta}}{\mu_{\perp} + \beta/\eta} Z\left(z\sqrt{\mu_{\parallel} + \frac{\beta}{\eta}}\right), \end{aligned} \quad (10)$$

where  $Z(\zeta)$  is the well-known Fried & Conte function (see Appendix B). We also need the derivative  $Z_{\kappa}^{(\eta, \zeta, \mu)'}(z) = dZ_{\kappa}^{(\eta, \zeta, \mu)}(z)/dz$ , which is

$$\begin{aligned} Z_{\kappa}^{(\eta, \zeta, \mu)'}(z) &= \frac{\eta^{-3/2}}{\mathcal{U}(\eta, \zeta, \mu)} \frac{1}{\Gamma(\zeta)} \\ &\times \int_0^{\infty} d\beta \frac{\sqrt{\mu_{\parallel} + \beta/\eta}}{\mu_{\perp} + \beta/\eta} \beta^{\zeta-1} e^{-\beta} Z'\left(z\sqrt{\mu_{\parallel} + \frac{\beta}{\eta}}\right). \end{aligned} \quad (11)$$

While the dispersion functions (10) and (11) depend solely on the anisotropy of the regularization parameters, there appears, additionally, another dispersion function which depends on the effects of all anisotropies: on the thermal speed parameters ( $\theta_{\parallel}, \theta_{\perp}$ ) and on the regularization parameters ( $\mu_{\parallel}, \mu_{\perp}$ ). Specifically,

$$\begin{aligned} \mathcal{Z}_{\kappa, \theta}^{(\eta, \zeta, \mu)}(z) &= \frac{\eta^{-3/2}}{\mathcal{U}(\eta, \zeta, \mu)} \frac{1}{\Gamma(\zeta)} \\ &\times \int_0^{\infty} d\beta \frac{\mathcal{A}_{\theta}^{\mu}(\beta) \beta^{\zeta-1} e^{-\beta}}{(\mu_{\perp} + \beta/\eta)(\mu_{\parallel} + \beta/\eta)} Z\left(z\sqrt{\mu_{\parallel} + \frac{\beta}{\eta}}\right), \end{aligned} \quad (12)$$

which depends on the global anisotropy function

$$\mathcal{A}_{\theta}^{\mu}(\beta) = 1 - \frac{\phi_{\perp}^2(\beta)}{\phi_{\parallel}^2(\beta)} = 1 - (1 - A_{\theta}) \frac{\mu_{\parallel} + \beta/\eta}{\mu_{\perp} + \beta/\eta}, \quad (13)$$

with  $A_{\theta} = 1 - \theta_{\perp}^2/\theta_{\parallel}^2$ . From the definition of  $\mathcal{Z}_{\kappa, \theta}^{(\eta, \zeta, \mu)}(z)$ , we need to consider two special cases. The first is the derivative  $\mathcal{Z}_{\kappa, \theta}^{(\eta, \zeta, \mu)'}(z) = d\mathcal{Z}_{\kappa, \theta}^{(\eta, \zeta, \mu)}(z)/dz$ , given by

$$\begin{aligned} \mathcal{Z}_{\kappa, \theta}^{(\eta, \zeta, \mu)'}(z) &= \frac{\eta^{-3/2}}{\mathcal{U}(\eta, \zeta, \mu)} \frac{1}{\Gamma(\zeta)} \\ &\times \int_0^{\infty} d\beta \frac{\mathcal{A}_{\theta}^{\mu}(\beta) \beta^{\zeta-1} e^{-\beta}}{(\mu_{\perp} + \beta/\eta)\sqrt{\mu_{\parallel} + \beta/\eta}} Z'\left(z\sqrt{\mu_{\parallel} + \frac{\beta}{\eta}}\right). \end{aligned} \quad (14)$$

The other relevant case is the  $\mu$ -isotropic limit of (14), which reduces to

$$\mathcal{Z}_{\kappa, \theta}^{(\eta, \zeta, \mu)'}(z) = A_{\theta} \mathcal{Z}_{\kappa}^{(\eta, \zeta, \mu)'}(z), \quad (15a)$$

where

$$\begin{aligned} \mathcal{Z}_{\kappa}^{(\eta, \zeta, \mu)'}(z) &= \frac{\eta^{-3/2} (\eta\mu)^{3/2-\zeta}}{U(\zeta, \zeta-1/2, \eta\mu)} \frac{1}{\Gamma(\zeta)} \\ &\times \int_0^{\infty} d\beta \frac{\beta^{\zeta-1} e^{-\beta}}{(\mu + \beta/\eta)^{3/2}} Z'\left(z\sqrt{\mu + \frac{\beta}{\eta}}\right). \end{aligned} \quad (15b)$$

The representations (10) – (15) of the new dispersion functions in terms of improper integrals are enough for their numerical evaluation, as long as efficient routines for the evaluation of  $Z(\zeta)$  and its derivative on the entire complex plane are available. Nevertheless, the well-known mathematical properties of the Fried & Conte function allows one to derive additional representations for certain regions of the Argand plane of  $\zeta$ . Some of these properties will be derived below, respectively for expressions (10), (11), (14) and (15).

#### 1. Values at origin

Knowing that  $Z(0) = i\sqrt{\pi}$  and  $Z'(0) = -2$ , by setting  $z = 0$  in the sequence of dispersion functions and comparing the resulting integrals with the results in section A 1, we obtain

$$Z_{\kappa}^{(\eta, \zeta, \mu)}(0) = -i\sqrt{\frac{\pi}{\eta}} \frac{U(1, 2-\zeta, \eta\mu_{\perp})}{\mathcal{U}(\eta, \zeta, \mu)} \quad (16a)$$

$$Z_{\kappa}^{(\eta, \zeta, \mu)'}(0) = -\frac{2}{\eta} \frac{\mathcal{U}_{-1,0}^{(\eta, \zeta, \mu)}}{\mathcal{U}(\eta, \zeta, \mu)} \quad (16b)$$

$$\mathcal{Z}_{\kappa, \theta}^{(\eta, \zeta, \mu)'}(0) = -2 \left[ 1 - (1 - A_{\theta}) \frac{\mathcal{U}_{-1,1}^{(\eta, \zeta, \mu)}}{\mathcal{U}(\eta, \zeta, \mu)} \right] \quad (16c)$$

$$\mathcal{Z}_{\kappa}^{(\eta, \zeta, \mu)'}(0) = -2, \quad (16d)$$

where we have also used (13).

#### 2. Power series expansions

We take the power series expansions for the  $Z$  function and its derivative

$$\begin{aligned} Z(z) &= i\sqrt{\pi} e^{-z^2} - 2z \sum_{n=0}^{\infty} \frac{(-z^2)^n}{(3/2)_n}, \\ Z'(z) &= -2i\sqrt{\pi} z e^{-z^2} - 2 \sum_{n=0}^{\infty} \frac{(-z^2)^n}{(1/2)_n}, \end{aligned}$$

where  $(a)_n = \Gamma(a+n)/\Gamma(a)$  is the Pochhammer symbol, with  $\Gamma(z)$  being the gamma function. Inserting these expan-

sions into the representations (10), (11), (14) and (15), the ensuing integrals can be readily identified with the results obtained in Appendix A, resulting

$$Z_{\kappa}^{(\eta, \zeta, \boldsymbol{\mu})}(z) = -\frac{2z/\eta}{\mathcal{U}(\eta, \zeta, \boldsymbol{\mu})} \sum_{n=0}^{\infty} \frac{\mathcal{U}_{-n-1,0}^{(\eta, \zeta, \boldsymbol{\mu})}}{(3/2)_n} \left(-\frac{z^2}{\eta}\right)^n + iZ_{\kappa, C}^{(\eta, \zeta, \boldsymbol{\mu})}(z) \quad (17a)$$

$$Z_{\kappa}^{(\eta, \zeta, \boldsymbol{\mu})'}(z) = -\frac{2\eta^{-1}}{\mathcal{U}(\eta, \zeta, \boldsymbol{\mu})} \sum_{n=0}^{\infty} \frac{\mathcal{U}_{-n-1,0}^{(\eta, \zeta, \boldsymbol{\mu})}}{(1/2)_n} \left(-\frac{z^2}{\eta}\right)^n + iZ_{\kappa, C}^{(\eta, \zeta, \boldsymbol{\mu})'}(z) \quad (17b)$$

$$\mathcal{Z}_{\kappa, \boldsymbol{\theta}}^{(\eta, \zeta, \boldsymbol{\mu})'}(z) = -\frac{2}{\mathcal{U}(\eta, \zeta, \boldsymbol{\mu})} \sum_{n=0}^{\infty} \frac{\mathcal{V}_n^{(\eta, \zeta, \boldsymbol{\mu})}}{(1/2)_n} \left(-\frac{z^2}{\eta}\right)^n + i\mathcal{Z}_{\kappa, \boldsymbol{\theta}, C}^{(\eta, \zeta, \boldsymbol{\mu})'}(z) \quad (17c)$$

$$\mathcal{Z}_{\kappa}^{(\eta, \zeta, \boldsymbol{\mu})'}(z) = -2 \sum_{n=0}^{\infty} \frac{U(\zeta, \zeta - 1/2 + n, \eta\boldsymbol{\mu})}{U(\zeta, \zeta - 1/2, \eta\boldsymbol{\mu})} \frac{(-\boldsymbol{\mu}z^2)^n}{(1/2)_n} + i\mathcal{Z}_{\kappa}^{(\eta, \zeta, \boldsymbol{\mu})'}(z), \quad (17d)$$

where

$$\mathcal{V}_n^{(\eta, \zeta, \boldsymbol{\mu})} = \mathcal{U}_{-n,0}^{(\eta, \zeta, \boldsymbol{\mu})} - (1 - A_{\boldsymbol{\theta}}) \mathcal{U}_{-n-1,1}^{(\eta, \zeta, \boldsymbol{\mu})}.$$

In (17a-d), we have also introduced the functions

$$Z_{\kappa, C}^{(\eta, \zeta, \boldsymbol{\mu})}(z) = \sqrt{\pi\boldsymbol{\mu}_{\perp}} \frac{(\eta\boldsymbol{\mu}_{\perp})^{\zeta-3/2}}{\mathcal{U}(\eta, \zeta, \boldsymbol{\mu})} e^{-\boldsymbol{\mu}_{\parallel}z^2} U\left(\zeta, \zeta, \eta\boldsymbol{\mu}_{\perp} \left(1 + \frac{z^2}{\eta}\right)\right) \quad (18a)$$

$$Z_{\kappa, C}^{(\eta, \zeta, \boldsymbol{\mu})'}(z) = -\frac{2\sqrt{\pi}\eta^{-1}}{\mathcal{U}(\eta, \zeta, \boldsymbol{\mu})} \frac{z}{\sqrt{\eta}} e^{-\boldsymbol{\mu}_{\parallel}z^2} \left[ \left(1 + \frac{z^2}{\eta}\right)^{-\zeta} - (\eta\boldsymbol{\mu}_{\perp})^{\zeta} \mathcal{A}_{\boldsymbol{\mu}} U\left(\zeta, \zeta, \eta\boldsymbol{\mu}_{\perp} \left(1 + \frac{z^2}{\eta}\right)\right) \right] \quad (18b)$$

$$\mathcal{Z}_{\kappa, \boldsymbol{\theta}, C}^{(\eta, \zeta, \boldsymbol{\mu})'}(z) = -2\sqrt{\pi} \frac{(\eta\boldsymbol{\mu}_{\perp})^{\zeta-1}}{\mathcal{U}(\eta, \zeta, \boldsymbol{\mu})} \frac{z}{\sqrt{\eta}} e^{-\boldsymbol{\mu}_{\parallel}z^2} \left[ A_{\boldsymbol{\theta}} U\left(\zeta, \zeta, \eta\boldsymbol{\mu}_{\perp} \left(1 + \frac{z^2}{\eta}\right)\right) + \mathcal{A}_{\boldsymbol{\mu}} (1 - A_{\boldsymbol{\theta}}) U\left(\zeta, \zeta - 1, \eta\boldsymbol{\mu}_{\perp} \left(1 + \frac{z^2}{\eta}\right)\right) \right] \quad (18c)$$

$$\mathcal{Z}_{\kappa, C}^{(\eta, \zeta, \boldsymbol{\mu})'}(z) = -2\sqrt{\pi\boldsymbol{\mu}z} e^{-\boldsymbol{\mu}z^2} \frac{U(\zeta, \zeta, \eta\boldsymbol{\mu} (1 + z^2/\eta))}{U(\zeta, \zeta - 1/2, \eta\boldsymbol{\mu})}. \quad (18d)$$

### 3. Asymptotic expansions

Similarly, we start from the known asymptotic expansions

$$Z(z) \sim -\frac{1}{z} \sum_{k=0}^{\infty} \frac{(1/2)_k}{z^{2k}} + \sigma i\sqrt{\pi} e^{-z^2}, \quad Z'(z) \sim \sum_{k=0}^{\infty} \frac{(3/2)_k}{z^{2(k+1)}} - 2\sigma i\sqrt{\pi} z e^{-z^2}, \quad \text{where } \sigma = \begin{cases} 0, & \Im z > 0 \\ 1, & \Im z = 0 \\ 2, & \Im z < 0. \end{cases}$$

Proceeding in a similar manner as in the previous sections, we obtain the following asymptotic expansions

$$Z_{\kappa}^{(\eta, \zeta, \boldsymbol{\mu})}(z) \sim -\frac{1}{z} \sum_{k=0}^{\infty} \binom{1}{2}_k \frac{\mathcal{U}_{k,0}^{(\eta, \zeta, \boldsymbol{\mu})}}{\mathcal{U}(\eta, \zeta, \boldsymbol{\mu})} \left(\frac{\eta}{z^2}\right)^k + \sigma i Z_{\kappa, C}^{(\eta, \zeta, \boldsymbol{\mu})}(z)$$

$$Z_{\kappa}^{(\eta, \zeta, \boldsymbol{\mu})'}(z) \sim \frac{1}{z^2} \sum_{k=0}^{\infty} \binom{3}{2}_k \frac{\mathcal{U}_{k,0}^{(\eta, \zeta, \boldsymbol{\mu})}}{\mathcal{U}(\eta, \zeta, \boldsymbol{\mu})} \left(\frac{\eta}{z^2}\right)^k + \sigma i Z_{\kappa, C}^{(\eta, \zeta, \boldsymbol{\mu})'}(z)$$

$$\mathcal{Z}_{\kappa, \boldsymbol{\theta}}^{(\eta, \zeta, \boldsymbol{\mu})'}(z) \sim \frac{\eta}{z^2} \sum_{k=0}^{\infty} \binom{3}{2}_k \left[ \frac{\mathcal{U}_{k+1,0}^{(\eta, \zeta, \boldsymbol{\mu})}}{\mathcal{U}(\eta, \zeta, \boldsymbol{\mu})} - (1 - A_{\boldsymbol{\theta}}) \frac{\mathcal{U}_{k,1}^{(\eta, \zeta, \boldsymbol{\mu})}}{\mathcal{U}(\eta, \zeta, \boldsymbol{\mu})} \right] \left(\frac{\eta}{z^2}\right)^k + \sigma i \mathcal{Z}_{\kappa, \boldsymbol{\theta}, C}^{(\eta, \zeta, \boldsymbol{\mu})'}(z)$$

$$\mathcal{Z}_\kappa^{(\eta,\zeta,\mu)'}(z) \sim \frac{\eta}{z^2} \sum_{k=0} \binom{3}{2}_k \frac{U(5/2+k, 7/2+k-\zeta, \mu\eta)}{U(3/2, 5/2-\zeta, \eta\mu)} \left(\frac{\eta}{z^2}\right)^k + \sigma i \mathcal{Z}_{\kappa,C}^{(\eta,\zeta,\mu)'}(z),$$

valid for  $|z| \gg \sqrt{\eta}$ , also in terms of the functions (18a-d).

### III. INSTABILITIES FROM SEMI-ANISOTROPIC DISTRIBUTIONS

The expressions derived in Sec. II will now be applied to the study of wave instabilities arising due to nonthermal features in the electron VDF, such as temperature anisotropies and drift speeds. We examine the instabilities of electromagnetic, circularly-polarized modes given by the solutions of the dispersion equation (8).

We assume a plasma of electrons and ions (mostly protons) typical of the solar wind, often described with a three-component electron population: at low energies the core described by a dbM VDF, a more tenuous suprathermal halo, a beam or strahl component. For simplicity - and supported by recent observations in the young solar wind<sup>40</sup> - here we neglect the halo component, adopting instead a two-component electron VDF comprising the core (subscript  $c$ ) plus the strahl (subscript  $s$ ):

$$f_e(v_{\parallel}, v_{\perp}) = \frac{n_c}{n} f_c(v_{\parallel}, v_{\perp}) + \frac{n_s}{n} f_s(v_{\parallel}, v_{\perp}). \quad (20)$$

The relative densities and drift speeds satisfy the usual constraints of zero net charge  $n_i = n_e = n_c + n_s$  and zero current density  $n_c U_{\parallel c} + n_s U_{\parallel s} = 0$ . The dispersion equation will be solved in the ion's rest frame ( $U_{\parallel i} = 0$ ).

The components of the susceptibility tensor (6a-c) will be analytically evaluated for the core-strahl model (20). The strahl population will be modelled by a drifting bi-RKD (1), identified by the acronym dbRK. For this population, the partial susceptibilities are given by Eqs. (9a, b), evaluated with the new dispersion functions (10) and (14). The susceptibility tensor components for the dbM core can be found in the literature and are listed in Appendix B. Since we are interested in the instabilities driven by free energy sources contained in the electronic component of the plasma, the ion contribution is not relevant for this study, and so they will be modelled by an isotropic Maxwellian distribution, see (3) with  $U_{\parallel} = 0$  and  $\theta_{\parallel} = \theta_{\perp}$ .

Once the total susceptibility tensor of the core-strahl system is evaluated, the dispersion equation (8) is numerically solved in order to provide the complex function

$$\omega(k_{\parallel}) = \omega_r(k_{\parallel}) + i\gamma(k_{\parallel}),$$

with the wave frequency dispersion relation  $\omega_r(k_{\parallel})$  for the  $R$  and  $L$  circularly-polarized modes, and the associated damping/growth rates  $\gamma(k_{\parallel})$ . This approach is called here *semi-analytic* and this is the first time it is applied to analyse kinetic instabilities excited by anisotropic RKDs.

The semi-analytic approach will be complemented by one employing the Arbitrary Linear Plasma Solver (ALPS),<sup>36</sup>

which is a parallelized numerical solver, developed in Modern Fortran, that computes solutions to the most general dispersion relation under a wide range of plasma conditions, including both hot non-relativistic and relativistic regimes. Its flexibility enables the treatment of an arbitrary number of particle species with equilibrium distribution functions  $f_{0j}$ , and it allows for any propagation direction relative to the unperturbed background magnetic field. To run ALPS, one merely needs to provide numerical input for the equilibrium distributions  $f_{0,j}(p_{\perp}, p_{\parallel})$ , where  $p_{\parallel}$  and  $p_{\perp}$  represent the momentum components parallel and perpendicular to the background field. Moreover, initial guesses for the real  $\omega_r$  and imaginary  $\gamma$ , must be specified. The code applies an iterative Newton-secant scheme, yielding the dispersion relation in terms of  $\omega_r(\mathbf{k})$  and  $\gamma(\mathbf{k})$ . Further details on the implementation and functionality of ALPS and its applicability can be found in Refs 32, 33, 36, and 41. Note, in particular, that ALPS is not informed about any specific form of the VDFs and, therefore, its 'fully numerical' results are excellent tests for those obtained with the semi-analytical approach.

The excitation of wave instabilities will be first studied for a strahl population modelled by a dbRK VDF with temperature anisotropy ( $T_{\perp s} \neq T_{\parallel s}$ ), but with isotropic regularization ( $\mu_{\perp s} = \mu_{\parallel s} = \mu$ ), a situation already analyzed by Ref. 33, but employing solely a purely numerical approach with the ALPS code. In all cases, the parameters in the generalized expression (1) were fixed to  $\eta = \kappa$ , and  $\zeta = \kappa + 1$ . Each population is described by the following nondimensional quantities

$$\beta_a = \frac{4\pi n_a m_a \theta_{\parallel a}^2}{B_0^2}, \quad u_s = \frac{U_{\parallel s}}{c_l}, \quad \eta = \frac{n_s}{n_e}, \quad r_{Ta} = \frac{T_{\perp a}}{T_{\parallel a}},$$

where  $\beta_a$  is the beta parameter for population  $a$  ( $a = c, s$ ),  $B_0$  is the magnetic field and  $c_l$  is the speed of light in vacuum. Here, we adopt  $\eta$  for the density ratio, since the homonymous parameter in Eq. (1) is already set equal to  $\kappa$ . It is also worth pointing out that in the present case, according to (5) and (A10), the temperature ratio  $r_{Ta}$  is independent of the regularization parameter, similarly to what happens with a standard bi-Kappa distribution.

Instabilities generated by the electron strahl, which is very often the main heat-flux carrier in the solar wind, are known as heat-flux instabilities (HFIs). Here these unstable solutions will also accumulate the effects of the second source of free energy that is the temperature anisotropy. Figure 1 shows the results for the "pure" whistler heat-flux instability (WHFI), occurring in the  $R$  mode for isotropic temperature, ( $r_{Ti} = r_{Tc} = r_{Ts} = 1$ ). The sole free energy source resides in the relative core-strahl drift. Results obtained from the semi-analytical approach are depicted as continuous lines, whereas the ALPS results are identified by the dots. The left panel shows the frequency dispersion relations for each parameter

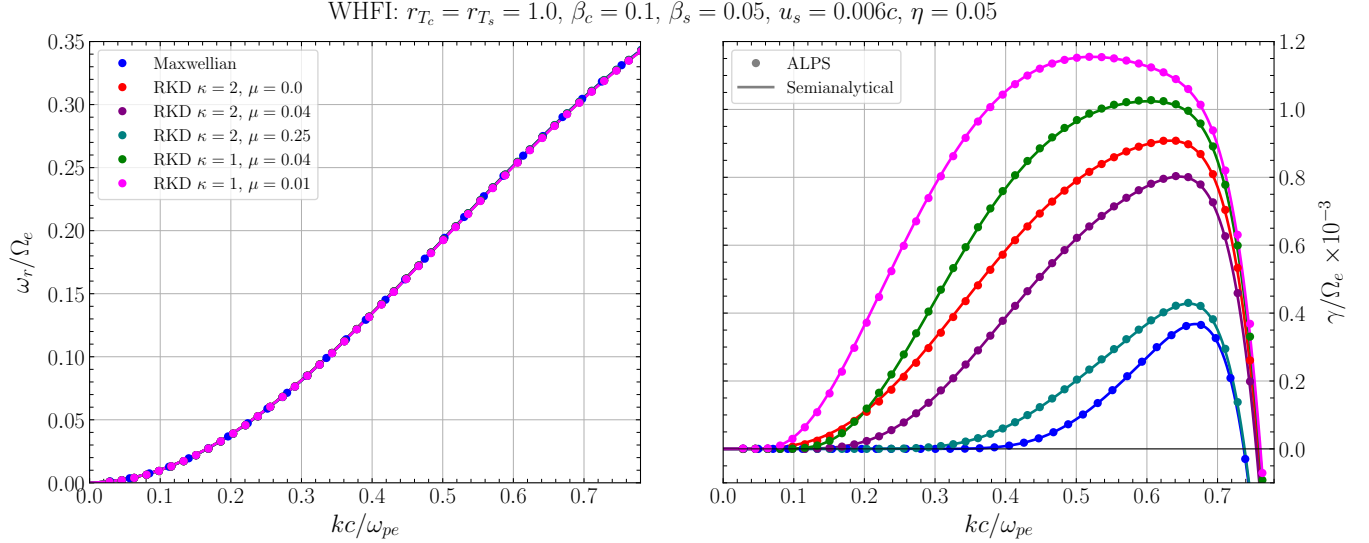


FIG. 1. Dispersion relations (left panel) and growth rates (right panel) of WHFI triggered by strahl populations with different values of the  $\kappa$  and the regularization parameter. Continuous lines were produced by the semi-analytical approach, whereas the dots are results obtained with ALPS. The same conventions and colors are adopted in the following figures.

set (indicated in the legend and specifically selected to trigger the instability), whereas the right panel shows the associated growth rates. In particular, notice that WHFI is excited by relatively slow beams ( $u_s = 0.006$ ).

The unstable solutions were obtained for several combinations of thermal or suprathermal parameters. In the first run (blue line and dots), the strahl component was modelled by a dbM VDF. In the semi-analytical approach, the corresponding  $\chi_{1,2}^{\text{dbM}}(\omega, k_{\parallel})$  tensor components were evaluated by Eqs. (B1a, b). One can observe that the instability is already present in the Maxwellian case. The red lines and dots depict the results from a strahl described by a drifting bi-Kappa (dbK) VDF, with  $\kappa = 2$  (close to the allowed minimum value of 1.5). The ALPS code reproduces this situation by setting the regularization parameter  $\mu = 0$  when the VDF grid is generated. For the semi-analytical approach, the dbK VDF (B2) was adopted. In this case, the  $\chi_{1,2}^{\text{dbK}}(\omega, k_{\parallel})$  tensor components are given by Eqs. (B3a, b). One can observe that the growth rate for the instability excited by a suprathermal plasma is always higher than that excited by a Maxwellian strahl.

The remaining plots show the WHFI excited by RKD strahls, and now the semi-analytical approach employs the new formulas developed here for the evaluation of the  $\chi_{1,2}^{\text{dbRK}}(\omega, k_{\parallel})$  components given by Eqs. (9a, b). The purple line and dots show the results for a dbRK VDF with the same value of  $\kappa = 2$ , but with a finite  $\mu = 0.04$ . Notice that the instability is somewhat smouldered as compared with the SKD result, due to the effect of the (relatively large) regularization parameter. The same trend can be observed in the cyan results, again obtained with  $\kappa = 2$  but with a larger  $\mu = 0.25$ . In this case, the instability is even more suppressed due to a less suprathermal nature of the RKD, within a lower energy range above which the VDF behaves basically as Maxwellian.

The opposite behavior is observed if the suprathermal fea-

ture of the strahl is increased. The green results are obtained for a lower  $\kappa = 1$  and  $\mu = 0.04$ , and now the VDF retains its suprathermality for larger energies, leading to enhanced growth rate, as compared to the pure dbK case. For a lower energy cut-off (at even higher levels), the strahl is able to generate stronger instabilities, as exemplified by the magenta results, where  $\kappa = 1$  and  $\mu = 0.01$ . In summary, the higher the suprathermality level in the strahl component, the higher the growth rates of the WHFI. On the other hand, the  $R$ -mode frequency in the left panel of Fig. 1 is completely unaffected by the thermal nature of the beam. The final worthwhile observation is the excellent agreement between the semi-analytical approach and the purely numerical results obtained from ALPS. This remarkable agreement serves to validate the results obtained from both approaches.

Figure 2 shows results obtained from a set of parameters able to generate the firehose heat-flux instability (FHFI), which occurs in the  $L$  mode. The FHFI needs relatively higher values of beta parameters and higher drift speeds than the WHFI. As above, the different results were generated by varying the degree of suprathermality of the strahl. The first noticeable feature is once more the excellent agreement between the results obtained from both approaches adopted in this work.

Differently from Fig. 1, though, we now observe that both the real ( $\omega_r$ ) and imaginary ( $\gamma$ ) parts of the solutions are greatly affected by the strahl's thermal level. The Maxwellian result (blue curve and dots) shows that the wave can exhibit growth at a relatively high spectral range ( $0.06 \lesssim kc/\omega_{pe} \lesssim 0.088$ ), while at the same time exhibits a region of negative phase velocity in the range  $0.035 \lesssim kc/\omega_{pe} \lesssim 0.06$ . However, a completely different picture emerges with a suprathermal strahl. The pure dbK case (red) with  $\kappa = 2$  shows that the instability is completely suppressed while at

FHFI:  $r_{T_c} = r_{T_s} = 1.0$ ,  $\beta_c = 1.2$ ,  $\beta_s = 0.6$ ,  $u_s = 0.036c$ ,  $\eta = 0.05$

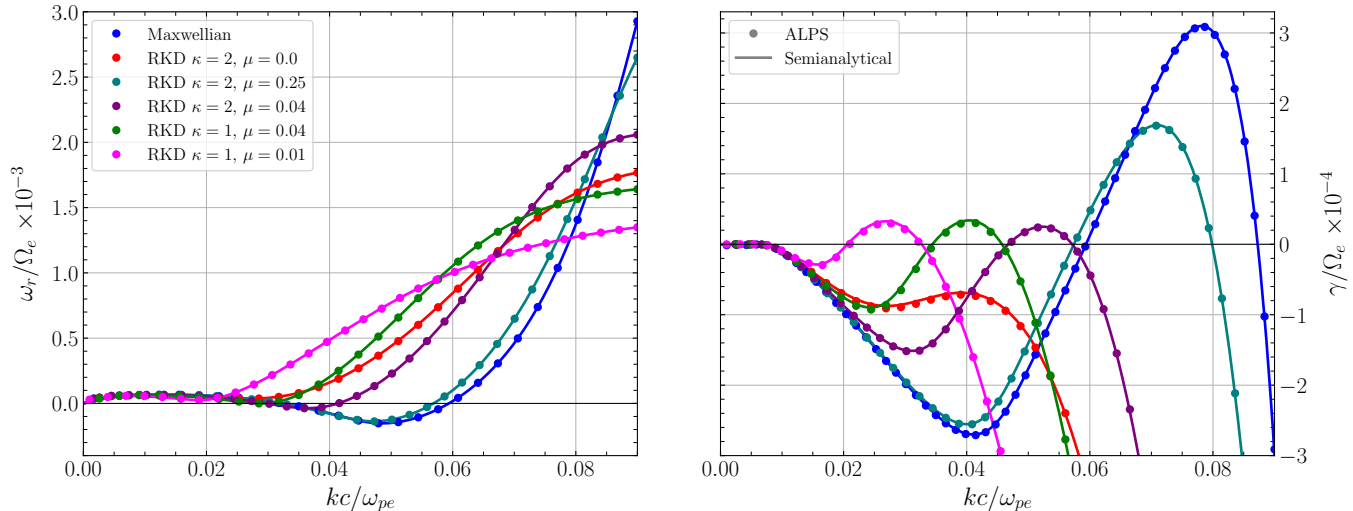


FIG. 2. FHFI in the  $L$  mode excited by a streaming strahl. The beam is still isotropic around the drift and the other parameters are set in order to excite the instability.

the same time the wave is forward-propagating throughout the spectral range. The Maxwellian result can then be recovered from a RKD strahl when the regularization parameter is high, as can be observed in the purple ( $\kappa = 2$ ,  $\mu = 0.04$ ) and cyan ( $\kappa = 2$ ,  $\mu = 0.25$ ) results, with which the thermal case can be asymptotically reproduced.

When the suprathermality of the strahl increases, a somewhat different picture emerges. The green ( $\kappa = 1$ ,  $\mu = 0.04$ ) and magenta ( $\kappa = 1$ ,  $\mu = 0.01$ ) results show that as the suprathermality level increases, the FHFI occurs in increasingly lower spectral ranges. The figure shows quite different results between the dbK and the dbRK cases, and these results suggest that the maximum growth rates and spectral ranges of the FHFI can depend quite differently on the level of suprathermality of the strahl.

Since the electrons observed in the solar wind also show conspicuous anisotropies in the VDF, it is worthwhile to add the effect of temperature anisotropy to the heat flux carried by the strahl. In this case the strahl will provide two free energy sources capable of triggering instabilities. A thorough analysis of the complex interplay between the effects of both energy sources was performed by Refs. 42 and 43 for the case when the strahl is modelled by a SKD. In the present work, we will only present some representative cases, but with a RKD strahl, reproducing the cases discussed by Ref. 33, which were obtained with the purely numerical approach.

The first case considers a beam with large perpendicular temperature ( $T_{\perp s} > T_{\parallel s}$ ), such as is the case of Fig. 3. Without drift ( $u_s = 0$ ), the electrons would typically excite the whistler instability acting on the right-handed ( $R$ ) circularly-polarized mode.<sup>12</sup> However, in the presence of a strong beam ( $u_s = 0.028$ ), the combined effect destabilizes the  $L$  mode.

While the dispersion relation (left panel) is weakly affected by changes of the RKD parameters, the right panel of Fig. 3 shows that the growth rate can be greatly enhanced. There are

already substantial increases in the maximum growth rate and in the breadth of the unstable spectral range due to the transition from Maxwellian (blue) to SKD (red), as in the previous examples. As in the previous cases, a RKD strahl can tend asymptotically back to the Maxwellian result if one increases the regularization parameter (purple and cyan results).

The opposite effect is once again obtained when one decreases the kappa parameter (to  $\kappa = 1$ ). The green ( $\mu = 0.04$ ) and magenta ( $\mu = 0.01$ ) plots in Fig. 3 show how extreme suprathermal strahls can fuel the instability.

As a final result in this section, Fig. 4 shows how inverting the temperature anisotropy to  $T_{\perp s} < T_{\parallel s}$  in combination with a moderate heat flux can still excite the  $L$  mode.

Without the drift, the anisotropy  $r_{T_s} < 1$  would equally excite the electron firehose instability in the  $L$  mode. The presence of a moderate beam speed can exacerbate the effect and changes on the suprathermality level of the strahl (beam) provoke even further modifications, this time in both  $\omega_r$  and  $\gamma$ .

A great leap is observed in the transition Maxwellian (blue)  $\rightarrow$  SKD (red). The dispersion relation of the latter case displays a steep slope in the short wavenumber region, while the growth rate also increases and moves to a lower spectral range. With a RKD beam, the results are roughly close to the SKD case, but can once more tend asymptotically back to the thermal situation. The only noticeable exception is shown by the purple curve, when the growth rate actually increases, before reducing back to the Maxwellian result.

#### IV. INSTABILITIES FROM FULLY ANISOTROPIC DISTRIBUTIONS

The cases analysed in Sec. III were restricted to the situation where the regularization parameter of the regularized dis-

WI+FHF1:  $r_{T_c} = 1.0$ ,  $r_{T_s} = 3.5$ ,  $\beta_c = 0.04$ ,  $\beta_s = 0.02$ ,  $u_s = 0.028c$ ,  $\eta = 0.05$

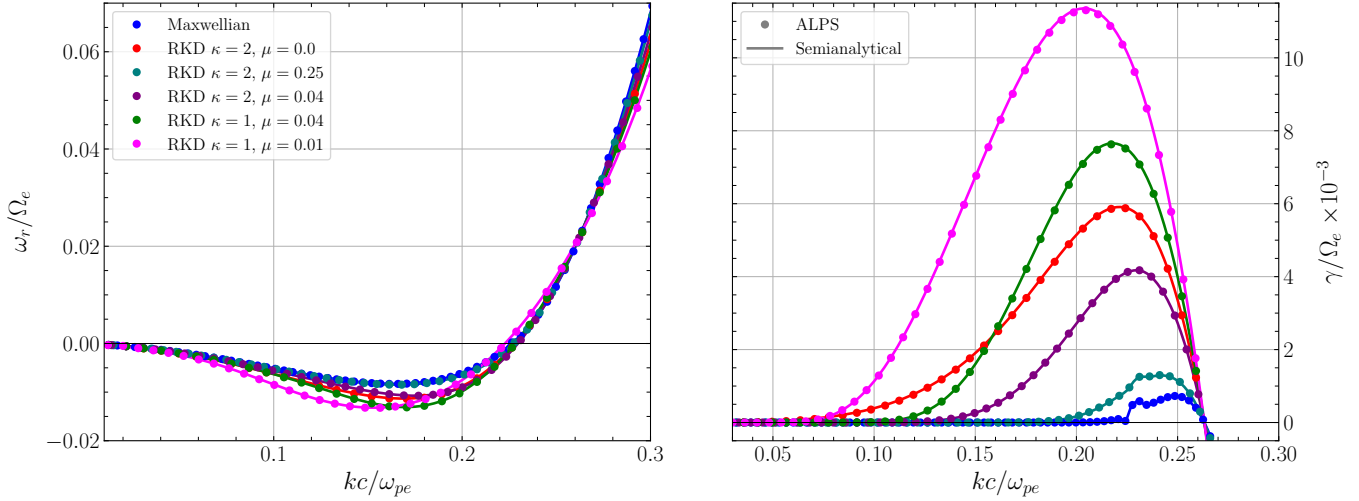


FIG. 3. Instability occurring in the  $L$  mode due to the combined effect of large heat flux and  $T_{\perp s} > T_{\parallel s}$  anisotropy.

EFH1:  $r_{T_c} = 1.0$ ,  $r_{T_s} = 0.2$ ,  $\beta_c = 4.0$ ,  $\beta_s = 2.0$ ,  $u_s = 0.005c$ ,  $\eta = 0.05$

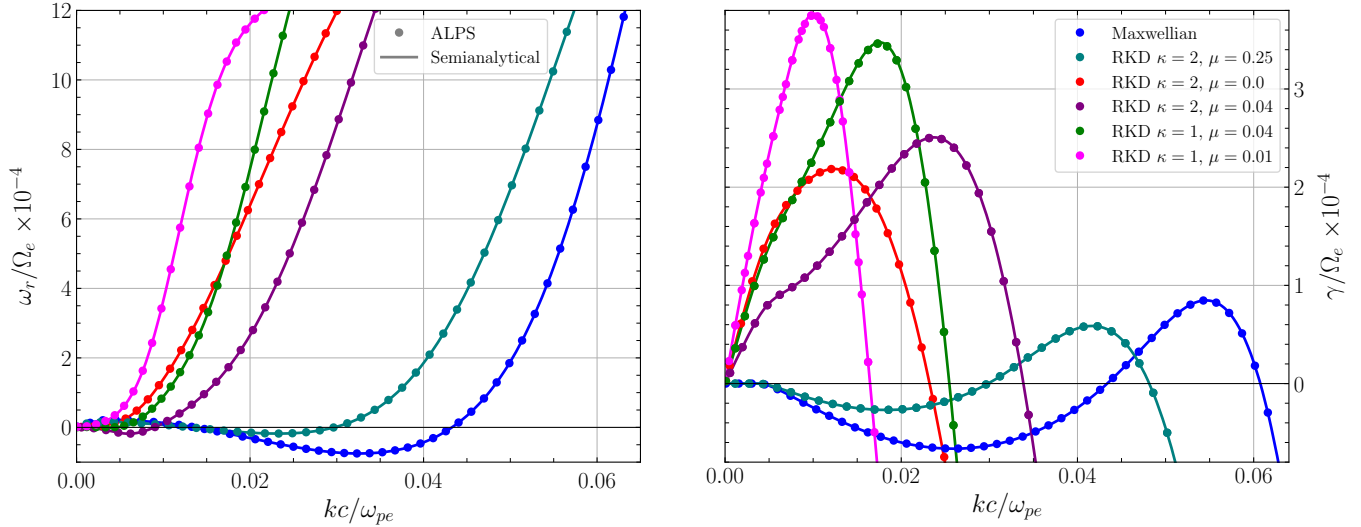


FIG. 4. Instability occurring in the  $L$  mode due to the combined effect of moderate heat flux and  $T_{\perp s} < T_{\parallel s}$  anisotropy.

tribution (1) is the same in both directions (*i. e.*,  $\mu_{\perp} = \mu_{\parallel} = \mu$ ). In this section, this limitation will be relaxed and the effects of anisotropies both in the thermal velocity spread parameters ( $\theta_{\perp} \neq \theta_{\parallel}$ ) and in the regularization parameter ( $\mu_{\perp} \neq \mu_{\parallel}$ ) will be considered.

As it was already pointed out, in the fully-anisotropic situation, the temperature ratio depends not only the thermal velocity spread parameters  $\theta_{\perp(\parallel)}$ , but also on the regularization parameters  $\mu_{\perp(\parallel)}$ . According to (5),

$$r_T = \frac{T_{\perp, \kappa, \theta}(\eta, \zeta, \mu)}{T_{\parallel, \kappa, \theta}(\eta, \zeta, \mu)} = \frac{\theta_{\perp}^2 \mathcal{W}_{0,1}(\eta, \zeta, \mu)}{\theta_{\parallel}^2 \mathcal{W}_{1,0}(\eta, \zeta, \mu)}.$$

Hence, in the following figures, we will provide for the strahl

component, instead of  $r_{T_s}$  (which was used for Maxwellian core and halo/strahl with semi-isotropic RKDs), the ratio

$$r_{\theta_s} = \frac{\theta_{\perp s}^2}{\theta_{\parallel s}^2}$$

and then evaluate the temperature ratio  $r_{T_s}$  from the formula above.

From a purely argumentative point of view, it stands to reason that the same forcing mechanisms responsible for the deformation of an otherwise perfectly isotropic VDF either on the parallel or on the perpendicular directions relative to the ambient magnetic field should act on the regularization parameter as well. Hence, although the inclusion of another (in

principle) free parameter to the distribution may seem at a first glance superfluous and unnecessary, a more faithful modelling of the observed distributions may in fact require including unequal  $\mu_{\perp}$  and  $\mu_{\parallel}$  in the analysis.

In this work, the effects of anisotropic  $\mu$ s on the heat flux instabilities are analysed for the first time, again with both semi-analytical and numerical approaches. The former is readily accomplished with the formulæ developed in Sec. II and Appendix A, whilst the latter is realized by setting  $\mu_{\parallel} \neq \mu_{\perp}$  when the VDF grid is created with the ALPS code.

In this first treatment, we will take the most extreme cases of suprathermal distributions considered in Figs. 1 – 4, namely, cases with  $\kappa = 1$ , and vary the values of  $\mu_{\perp}$  and  $\mu_{\parallel}$  around the reference value  $\mu = 0.01$ .

Figure 5 shows a case that reproduces the conditions that excite the whistler instability (WI) in the  $R$  mode only due to the anisotropy  $\theta_{\perp s} > \theta_{\parallel s}$ , without the supplemental free energy provided by a beam. This parameter set can reproduce the conditions in a core + halo system.

Since the dispersion relation is largely unaffected by the different cases, we will concentrate on the growth rate. The reference case  $\mu = 0.01$  is depicted by the black curve and dots. The WI is triggered by the larger dispersion of electron velocities in the perpendicular direction than in the parallel direction. Thus, an increase of  $\mu_{\perp}$  compared to  $\mu_{\parallel}$  will move the distribution's cut-off in the perpendicular direction to lower  $v_{\perp}$ , meaning that the degree of suprathermality of the distribution in that direction is reduced and it tends ever more to behave as a Maxwellian there, while retaining the original suprathermal characteristic in the parallel direction. Since a suprathermal plasma tends to support higher growth rates for the WI than a Maxwellian, we can in this way understand the effect depicted by the blue ( $\mu_{\perp} = 0.011$ ) and purple ( $\mu_{\perp} = 0.015$ ) curves in Fig. 5, which show a reduction in growth rate due to the increase of  $\mu_{\perp}$ , keeping  $\mu_{\parallel} = 0.01$ .

An alternative interpretation of these results is provided by the fact that an increase in  $\mu_{\perp}$  will effectively reduce the temperature anisotropy, thereby leading to lower growth rates for the whistler instability. This interpretation is corroborated by the depicted values of the temperature ratios: an increase of  $\mu_{\perp}$  results in a reduction of  $r_{Ts}$ , leading to smaller growth ratios.

The opposite effect is seen when  $\mu_{\perp} = 0.01$  is fixed and  $\mu_{\parallel}$  is increased, as is the case of the magenta ( $\mu_{\parallel} = 0.011$ ) and cyan ( $\mu_{\parallel} = 0.015$ ) results. The instability grows with  $\mu_{\parallel}$  and this behavior can be understood because in this case the effective anisotropy responsible for the WI is also increased (the temperature ratios increase).

The same straightforward explanation can not be trivially repeated when one considers situations conducive to the electron firehose instability (EFHI) acting on the  $L$  mode, such as those shown in Fig. 6. In this case, it was necessary to adopt a core + halo model for the ions as well, where the core is described by a Maxwellian, whereas the ion halo is given by an RKD. Both distributions are isotropic and the RKD parameters for the ions are  $\kappa_i = 1$  and  $\mu_i = 0.01$ . The parameters considered here are similar to those adopted in Fig. 7 of Ref. 32 and the physical parameters for all species ( $e, i$ ) and popu-

lations ( $c, h$ ) are clearly identified by the labels.

The reference case ( $\mu_{\perp e, h} = \mu_{\parallel e, h} = 1$ ) is again depicted by the black line and dots. The sequence of plots black  $\rightarrow$  green  $\rightarrow$  magenta  $\rightarrow$  purple  $\rightarrow$  red is obtained by a steady increase of  $\mu_{\parallel e, h}$  keeping  $\mu_{\perp e, h}$  fixed (*i.e.*, an increase in  $r_{Te, h}$ ). The observed consequence is a rightshift in both the dispersion relation and the growth rates. The former depicting a narrow range of almost zero group velocity, whereas the latter shifts keeping the maximum growth rate approximately constant, with a concomitant increase in the unstable spectral range.

A visible increase in the growth rate is only shown by the cyan results, where  $\mu_{\perp e, h} = 0.05$  was increased from the reference, keeping  $\mu_{\parallel e, h} = 0.01$ . In this case, the increase in  $\gamma$  can be interpreted as an enhancement of the effective anisotropy that gives rise to the electron firehose instability, which occurs when  $T_{\perp e, h} < T_{\parallel e, h}$ .

The analysis is concluded by returning to the standard situation of a single Maxwellian ion species and a core + strahl combination for the electrons, considering now two cases of instabilities excited by the interplay of temperature anisotropies with heat flux in the strahl. Figure 7 considers again the combination of heat flux with  $\theta_{\perp s} > \theta_{\parallel s}$  that generates instabilities in the  $L$  mode. The results take the most extreme combination of parameters in Fig. 3 ( $\kappa_s = 1$ ,  $\mu_s = 0.01$ ) and considers this the reference case. Similarly to what happened in Fig. 3, increasing  $\mu_{\parallel s}$  while keeping  $\mu_{\perp s}$  constant (results red and blue) can be interpreted as an enhancement on the effective temperature anisotropy that results in an increase of the instability, exactly as it happened with the pure WI shown in Fig. 3, but with the difference that now the instability occurs in the  $L$  mode. The opposite happens when  $\mu_{\perp s}$  increases keeping  $\mu_{\parallel s}$  fixed. The instability is increasingly suppressed in this situation.

Finally, Fig. 8 takes the parameters  $\kappa_s = 1$  and  $\mu_s = 0.01$  of Fig. 4, using them as the reference case for the excitation of the instability in the  $L$  mode occurring due to moderate heat flux combined with a  $\theta_{\perp s} < \theta_{\parallel s}$  anisotropy. The results show that the instability shuffles around the reference case for different anisotropies in the regularization parameter, with an apparent tendency of slowly shifting the peak to higher wavenumber whilst remaining largely at the same level, regardless of the anisotropy in the regularization parameter.

The results presented in Secs. III and IV were basically intended to demonstrate initial applications of the formalism developed in this work and by no means cover the full parameter space relevant to the considered instabilities. The most important outcome of the cases studied here is - based on the mutual validation provided by the excellent agreement between the results obtained with fully numerical treatment (employing the ALPS code) and those derived with the newly developed theoretical semi-analytical formalism - the new model describing the wave propagation and wave-particle interaction in fully anisotropic regularized kappa plasmas.

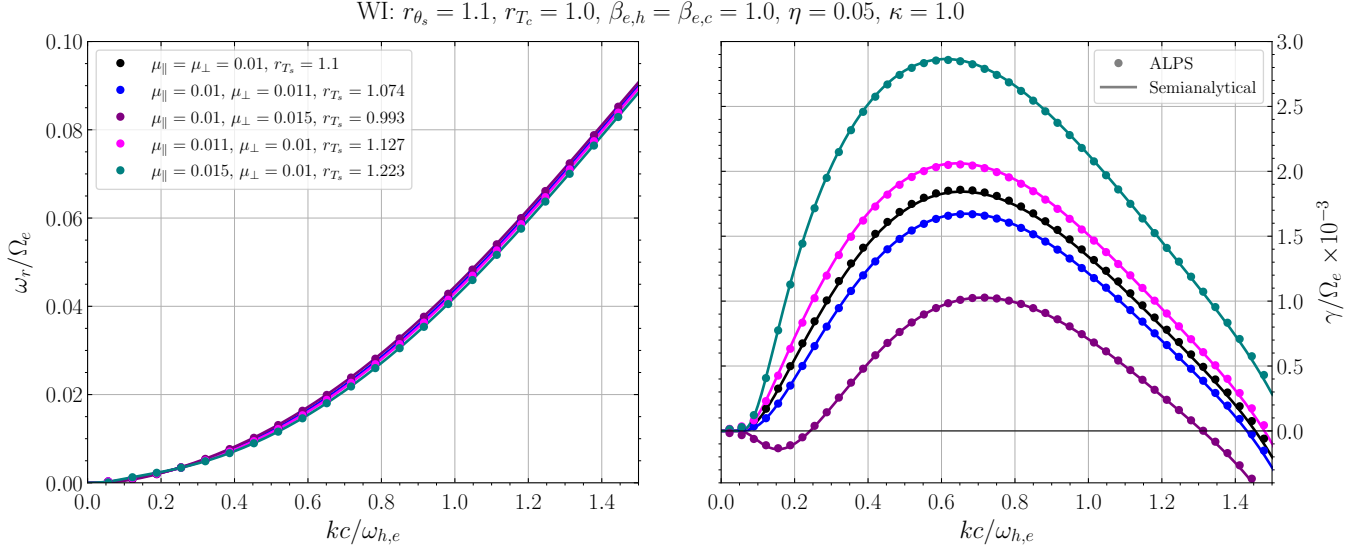


FIG. 5. Whistler instability generated by anisotropy  $r_{\theta_s} > 1$  in the strahl (or halo) when  $\kappa = 1$ , around the reference value  $\mu_{\perp s} = \mu_{\parallel s} = 0.01$ .

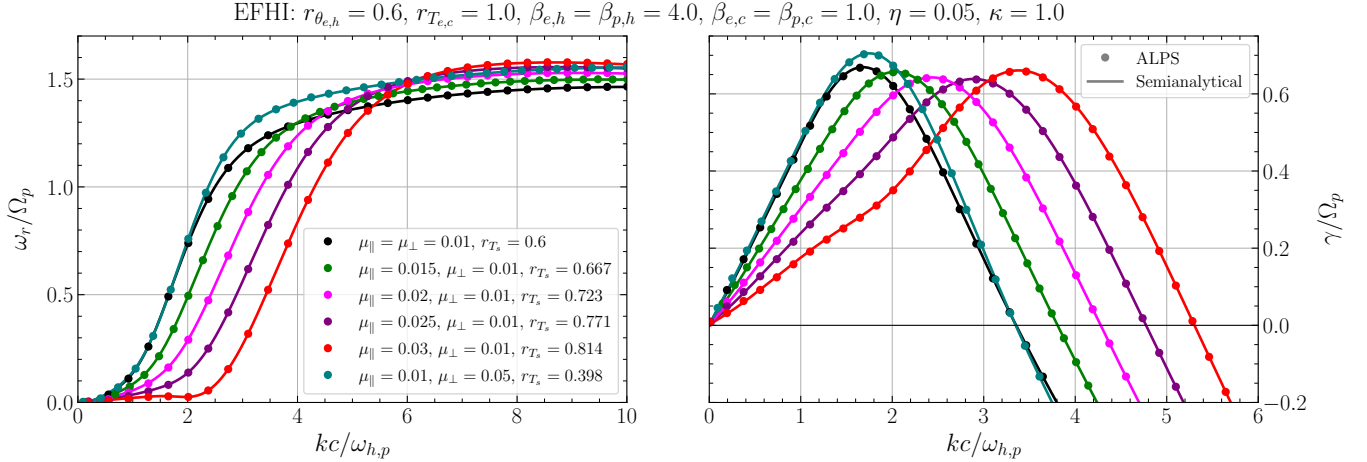


FIG. 6. Electron firehose instability generated by anisotropy  $r_{\theta_s} < 1$  in the electron halo when  $\kappa = 1$ , around the reference value  $\mu_{\perp h} = \mu_{\parallel h} = 0.01$ . Here, a core (Maxwellian) + halo (RKD,  $\kappa_i = 1$ ,  $\mu_i = 0.01$ ) model was also adopted for the ions. All populations are isotropic, except for the electron halo.

## V. SUMMARY AND CONCLUSIONS

In the present paper we provide a theoretical framework for studying wave instabilities in plasmas described by fully anisotropic RKDs, extending the (semi-)analytical foundations available for these type of distributions. We have defined new plasma dispersion functions for plasmas modelled by the fully anisotropic RKD, where the distribution's anisotropy manifests itself not only in different thermal velocity spreads between the parallel and perpendicular directions relative to the ambient magnetic field, but also in different cut-offs in these directions. Several important mathematical properties of these new dispersion functions have been derived, providing analytical expressions for the dielectric tensor components and the corresponding dispersion equations for both transver-

sal and longitudinal waves propagating parallel to the magnetic field. The dispersion equations for transverse, circularly-polarized parallel-propagating waves were numerically solved using two different approaches: semi-analytically, from the newly derived expressions in the present work and fully numerically by employing the dispersion solver ALPS. The relevant equations were solved employing realistic core + strahl and core + halo electron models, with physical parameters similar to those observed *in situ* in the solar wind, where both temperature anisotropy and heat-flux instabilities are observed. The dispersion relations and the growth rates obtained by either approach displayed excellent agreement in all adopted parameter sets, thus providing a mutual validation for both techniques and thereby demonstrating that the present formalism constitutes a reliable and versatile tool

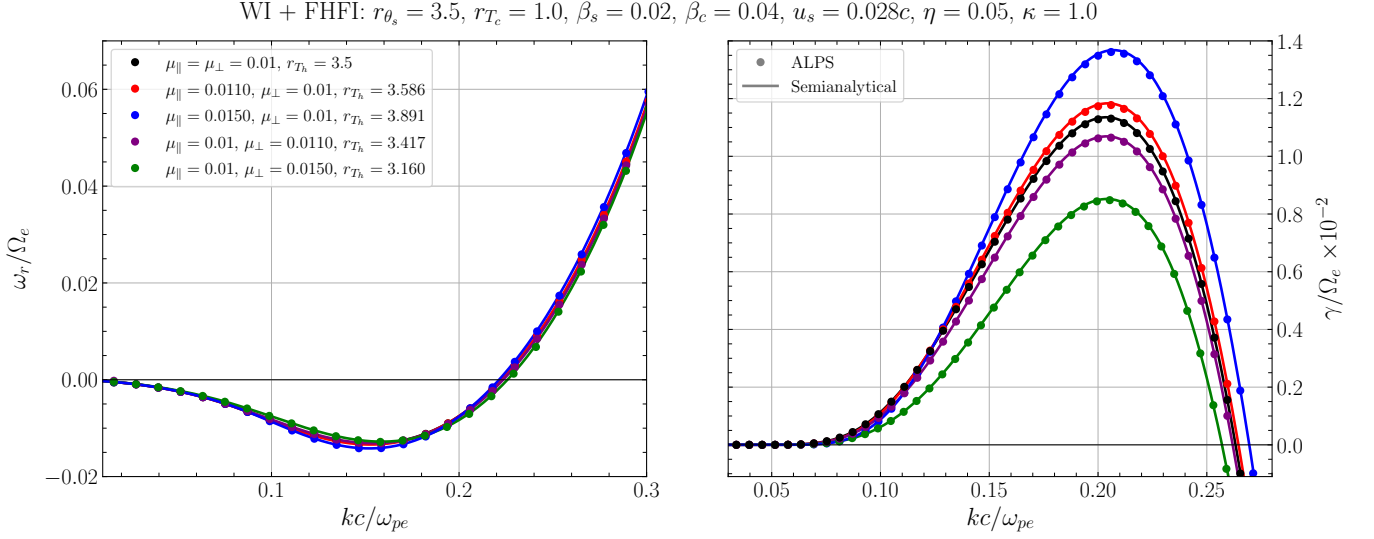


FIG. 7. Instability occurring in the  $L$  mode due to the combined effect of large heat flux and anisotropy  $r_{\theta_s} > 1$ . Results corresponding to the reference case  $\kappa = 1$  and  $\mu_{\perp s} = 0.01$  of Fig. 3, varying  $\mu_{\perp s} \neq \mu_{\parallel s}$ .

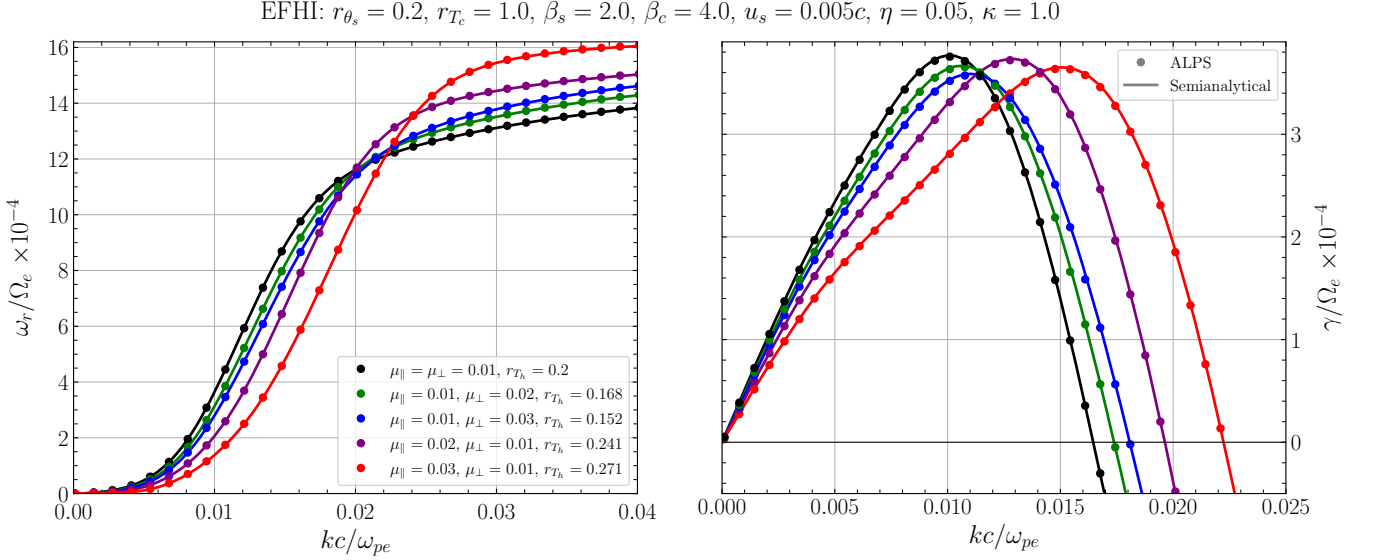


FIG. 8. Instability occurring in the  $L$  mode due to the combined effect of moderate heat flux and anisotropy  $r_{\theta_s} < 1$ . Results corresponding to the reference case  $\kappa = 1$  and  $\mu_{\perp s} = 0.01$  of Fig. 4, varying  $\mu_{\perp s} \neq \mu_{\parallel s}$ .

for the study of wave instabilities in plasmas described by anisotropic RKDs.

The results obtained when the distribution of suprathermal electrons featured both kinds of anisotropy, i.e. in the thermal velocity spread parameters and in the regularization parameters, demonstrate how such regularization can, depending on the nature of the instability and on the relative difference between the parallel and perpendicular cut-offs, act either as a stabilization that suppresses unstable modes or provide an additional source of free energy, thus enhancing the growth rates. These results indicate that the regularization parameters are not merely mathematical tools used to control the high-

energy tails and the effect of superluminal particles (always present in a non-relativistic treatment) of the distribution, but represent physically well-motivated quantities capable of influencing wave-particle interactions and energy transport.

The above findings overcome the inherent limitations of SKDs and significantly extend previous studies that were restricted to either purely numerical studies of anisotropic RKDs or semi-analytical derivations of isotropic RKDs. Given the widespread occurrence of suprathermal populations in various space plasma environments, such as the solar corona, solar wind, or planetary magnetospheres, our results contribute to a more realistic physical description of wave-

particle interaction and wave propagation in these environments and provide valuable benchmarks for future numerical, quasi-linear as well as observational studies.

## ACKNOWLEDGMENTS

We gratefully acknowledge financial support from DFG for a Mercator Fellowship for R.G., who also acknowledges support provided by Conselho Nacional de Desenvolvimento Científico e Tecnológico (CNPq), Grant No. 313330/2021-2. The research was funded within the WEAVE scheme by the Deutsche Forschungsgesellschaft (DFG), Project No. FI 706/31-1, and the Belgian FWO-Vlaanderen, project G002523N. The authors acknowledge the use of the ALPS code.

## Appendix A: Definitions and properties of integrals and special functions

In this appendix, we discuss some representations for the frequently-appearing integral  $I_{\beta}^{(p_1, p_2)}(\mu_{\parallel}, \mu_{\perp}, z)$ , defined by

$$I_{\beta}^{(p_1, p_2)} = \int_0^{\infty} \frac{\beta^{\zeta-1} e^{-(1+z^2/\eta)\beta} d\beta}{(\mu_{\parallel} + \beta/\eta)^{p_1} (\mu_{\perp} + \beta/\eta)^{p_2}}. \quad (\text{A1})$$

Equivalent forms for (A1) can be obtained depending on whether  $\mu_{\perp} > \mu_{\parallel}$  or  $\mu_{\perp} < \mu_{\parallel}$  and whether  $z = 0$  or  $z \neq 0$ . Here, we derive generic expressions for the case  $z = 0$ , whereas for the case  $z \neq 0$  we only need the cases  $p_1 = -1, 0$ .

Now, in the anisotropic case, we can derive power series expansions, valid when the anisotropy parameters are small. When  $|\mathcal{A}_{\mu}| < 1$ , we can employ the binomial theorem and expand in (A2b),

$$\frac{1}{(1+t-\mathcal{A}_{\mu})^{p_1}} = \frac{1}{(1+t)^{p_1}} \sum_{\ell=0}^{\infty} \frac{(p_1)_{\ell}}{\ell!} \left( \frac{\mathcal{A}_{\mu}}{1+t} \right)^{\ell},$$

In this case, we obtain

$$I_{\beta}^{(p_1, p_2)}(\mu_{\parallel}, \mu_{\perp}, 0) = \frac{(\eta\mu_{\perp})^{\zeta}}{\mu_{\perp}^{p_1+p_2}} \Gamma(\zeta) \sum_{\ell=0}^{\infty} \frac{(p_1)_{\ell}}{\ell!} U(\zeta, \zeta+1-p_1-p_2-\ell, \eta\mu_{\perp}) \mathcal{A}_{\mu}^{\ell}, \quad (\text{A6a})$$

where we have identified the Tricomi function in (A4) again.

### 1. Case $z = 0$

This is the simplest case, when (A1) reduces to

$$I_{\beta}^{(p_1, p_2)}(0) = \int_0^{\infty} \frac{\beta^{\zeta-1} e^{-\beta} d\beta}{(\mu_{\parallel} + \beta/\eta)^{p_1} (\mu_{\perp} + \beta/\eta)^{p_2}}. \quad (\text{A2a})$$

If we transform the integration variable to  $\beta = \eta\mu_{\perp}t$ , then

$$I_{\beta}^{(p_1, p_2)}(0) = \frac{(\eta\mu_{\perp})^{\zeta}}{\mu_{\perp}^{p_1+p_2}} \int_0^{\infty} dt \frac{t^{\zeta-1} e^{-\eta\mu_{\perp}t}}{(1+t-\mathcal{A}_{\mu})^{p_1} (1+t)^{p_2}}. \quad (\text{A2b})$$

On the other hand, if we define  $\beta = \eta\mu_{\parallel}t$ , then

$$I_{\beta}^{(p_1, p_2)}(0) = \frac{(\eta\mu_{\parallel})^{\zeta}}{\mu_{\parallel}^{p_1+p_2}} \int_0^{\infty} dt \frac{t^{\zeta-1} e^{-\eta\mu_{\parallel}t}}{(1+t)^{p_1} (1+t-A_{\mu})^{p_2}}. \quad (\text{A2c})$$

In (A2a, b) we have defined the anisotropy parameters

$$A_{\mu} = 1 - \frac{\mu_{\perp}}{\mu_{\parallel}}, \quad \mathcal{A}_{\mu} = 1 - \frac{\mu_{\parallel}}{\mu_{\perp}}, \quad (\text{A3})$$

which are related by

$$\mathcal{A}_{\mu} = \frac{A_{\mu}}{A_{\mu}-1}, \quad A_{\mu} = \frac{\mathcal{A}_{\mu}}{\mathcal{A}_{\mu}-1}.$$

The integral  $I_{\beta}^{(p_1, p_2)}(\mu_{\parallel}, \mu_{\perp}, 0)$  can be evaluated via numerical quadrature routines, but additional representations are possible. We start by noticing that when the regularization parameters are isotropic ( $\mu_{\parallel} = \mu_{\perp} = \mu$ ), (A2b) reduces to

$$I_{\beta}^{(p_1, p_2)}(\mu) = \frac{(\eta\mu)^{\zeta}}{\mu^{p_1+p_2}} \int_0^{\infty} dt \frac{t^{\zeta-1} e^{-\eta\mu t}}{(1+t)^{p_1+p_2}}.$$

Given the definition of the Tricomi function  $U(a, b, z)$ ,<sup>44</sup>

$$U(a, b, z) = \frac{1}{\Gamma(a)} \int_0^{\infty} dt t^{a-1} (1+t)^{b-a-1} e^{-zt}, \quad (\text{A4})$$

valid when  $\Re a > 0$  and  $|\arg(z)| < \pi/2$ , we obtain

$$I_{\beta}^{(p_1, p_2)}(\mu) = \frac{(\eta\mu)^{\zeta}}{\mu^{p_1+p_2}} \Gamma(\zeta) U(\zeta, \zeta+1-p_1-p_2, \eta\mu). \quad (\text{A5})$$

On the other hand, when  $|A_{\boldsymbol{\mu}}| < 1$ , we can proceed in the same fashion with (A2c) and obtain the alternative expansion

$$I_{\beta}^{(p_1, p_2)}(\boldsymbol{\mu}_{\parallel}, \boldsymbol{\mu}_{\perp}, 0) = \frac{(\eta \boldsymbol{\mu}_{\parallel})^{\zeta}}{\boldsymbol{\mu}_{\parallel}^{p_1+p_2}} \Gamma(\zeta) \sum_{\ell=0}^{\infty} \frac{(p_2)_{\ell}}{\ell!} U(\zeta, \zeta+1-p_1-p_2-\ell, \eta \boldsymbol{\mu}_{\parallel}) A_{\boldsymbol{\mu}}^{\ell}. \quad (\text{A6b})$$

Notice that both series reduce to (A5) in the  $\boldsymbol{\mu}$ -isotropic limit.

The direct evaluation of  $I_{\beta}^{(p_1, p_2)}(\boldsymbol{\mu}_{\parallel}, \boldsymbol{\mu}_{\perp})$  from the definition (A2) requires the numerical computation of improper integrals. We can, alternatively, obtain representations involving definite integrals over a finite region. We start by defining the new parameter  $\mathcal{W}_{\alpha, \beta}^{(\eta, \zeta, \boldsymbol{\mu})}$  as

$$\mathcal{W}_{\alpha, \beta}^{(\eta, \zeta, \boldsymbol{\mu})} = \frac{\Gamma(\alpha + \beta + 3/2)}{\Gamma(\alpha + 1/2)\Gamma(\beta + 1)} \int_0^1 dx \begin{cases} x^{\alpha-1/2} (1-x)^{\beta} U\left(\alpha + \beta + \frac{3}{2}, \alpha + \beta + \frac{5}{2} - \zeta, \eta \boldsymbol{\mu}_{\perp} (1 - \mathcal{A}_{\boldsymbol{\mu}} x)\right), & \boldsymbol{\mu}_{\parallel} < \boldsymbol{\mu}_{\perp} \\ (1-x)^{\alpha-1/2} x^{\beta} U\left(\alpha + \beta + \frac{3}{2}, \alpha + \beta + \frac{5}{2} - \zeta, \eta \boldsymbol{\mu}_{\parallel} (1 - A_{\boldsymbol{\mu}} x)\right), & \boldsymbol{\mu}_{\parallel} > \boldsymbol{\mu}_{\perp}, \end{cases} \quad (\text{A7})$$

which is valid for  $\alpha > -1/2$  and  $\beta > -1$ , and where  $U(a, b, z)$  is again the Tricomi function (A4). Definition (A7) requires now the evaluation of Euler-type integrals.

It can be shown that the integral  $I_{\beta}^{(p_1, p_2)}(\boldsymbol{\mu}_{\parallel}, \boldsymbol{\mu}_{\perp})$  and the parameter  $\mathcal{W}_{\alpha, \beta}^{(\eta, \zeta, \boldsymbol{\mu})}$  are related by the identity

$$I_{\beta}^{(p_1, p_2)}(\boldsymbol{\mu}_{\parallel}, \boldsymbol{\mu}_{\perp}, 0) = \Gamma(\zeta) \eta^{p_1+p_2} \mathcal{W}_{p_1-1/2, p_2-1}^{(\eta, \zeta, \boldsymbol{\mu})}, \quad (\text{A8})$$

which is valid in both cases  $\boldsymbol{\mu}_{\parallel} < \boldsymbol{\mu}_{\perp}$  and  $\boldsymbol{\mu}_{\parallel} > \boldsymbol{\mu}_{\perp}$ .

In order to derive (A8), we introduce into (A2a) the identity

$$\frac{1}{A_1^{\alpha_1} A_2^{\alpha_2}} = \frac{\Gamma(\alpha_1 + \alpha_2)}{\Gamma(\alpha_1)\Gamma(\alpha_2)} \int_0^1 dx_1 \int_0^1 dx_2 \frac{x_1^{\alpha_1-1} x_2^{\alpha_2-1} \delta(1-x_1-x_2)}{(x_1 A_1 + x_2 A_2)^{\alpha_1+\alpha_2}},$$

known as Feynman parametrization, and which is valid for  $\alpha_1, \alpha_2 > 0$ . Restricting ourselves first to the particular case  $0 < \mathcal{A}_{\boldsymbol{\mu}} < 1$  ( $\boldsymbol{\mu}_{\parallel} < \boldsymbol{\mu}_{\perp}$ ), we can easily obtain

$$I_{\beta}^{(p_1, p_2)}(\boldsymbol{\mu}_{\parallel}, \boldsymbol{\mu}_{\perp}, 0) = \frac{\Gamma(p_1 + p_2) (\eta \boldsymbol{\mu}_{\perp})^{\zeta}}{\Gamma(p_1)\Gamma(p_2) \boldsymbol{\mu}_{\perp}^{p_1+p_2}} \int_0^1 dx x^{p_1-1} (1-x)^{p_2-1} (1 - \mathcal{A}_{\boldsymbol{\mu}} x)^{\zeta-p_1-p_2} \int_0^{\infty} dy \frac{y^{\zeta-1} e^{-\eta \boldsymbol{\mu}_{\perp} (1 - \mathcal{A}_{\boldsymbol{\mu}} x) y}}{(1+y)^{p_1+p_2}},$$

after changing the integration variable  $\beta \rightarrow y$  through  $\beta = \eta \boldsymbol{\mu}_{\perp} (1 - \mathcal{A}_{\boldsymbol{\mu}} x) y$ . Comparing the last integral with (A4) and then comparing the result with (A7), we obtain identity (A8). During the demonstration, we also employed the Kummer transformation<sup>44</sup>  $U(a, b, z) = z^{1-b} U(a-b+1, 2-b, z)$ . The demonstration for the case  $\boldsymbol{\mu}_{\parallel} > \boldsymbol{\mu}_{\perp}$  ( $0 < A_{\boldsymbol{\mu}} < 1$ ) proceeds in a similar fashion.

Finally, identity (A8) provides two additional expressions valid for any values of the parameters  $\alpha$  and  $\beta$ . Firstly, from (A6a, b) one obtains the expansions

$$\mathcal{W}_{\alpha, \beta}^{(\eta, \zeta, \boldsymbol{\mu})} = \begin{cases} (\eta \boldsymbol{\mu}_{\perp})^{\zeta-\alpha-\beta-3/2} \sum_{\ell=0}^{\infty} \frac{(\alpha+1/2)_{\ell}}{\ell!} U\left(\zeta, \zeta - \alpha - \beta - \frac{1}{2} - \ell, \eta \boldsymbol{\mu}_{\perp}\right) \mathcal{A}_{\boldsymbol{\mu}}^{\ell}, & |\mathcal{A}_{\boldsymbol{\mu}}| < 1 \\ (\eta \boldsymbol{\mu}_{\parallel})^{\zeta-\alpha-\beta-3/2} \sum_{\ell=0}^{\infty} \frac{(\beta+1)_{\ell}}{\ell!} U\left(\zeta, \zeta - \alpha - \beta - \frac{1}{2} - \ell, \eta \boldsymbol{\mu}_{\parallel}\right) A_{\boldsymbol{\mu}}^{\ell}, & |A_{\boldsymbol{\mu}}| < 1. \end{cases} \quad (\text{A9})$$

Secondly, from (A2a) we have the direct evaluation from the improper integral

$$\mathcal{W}_{\alpha_1, \alpha_2}^{(\eta, \zeta, \boldsymbol{\mu})} = \frac{1}{\Gamma(\zeta)} \eta^{-(\alpha_1+\alpha_2+3/2)} \int_0^{\infty} \frac{d\beta \beta^{\zeta-1} e^{-\beta}}{(\boldsymbol{\mu}_{\parallel} + \beta/\eta)^{\alpha_1+1/2} (\boldsymbol{\mu}_{\perp} + \beta/\eta)^{\alpha_2+1}}.$$

Important particular cases of  $\mathcal{W}_{\alpha, \beta}^{(\eta, \zeta, \boldsymbol{\mu})}$  can be also derived. The first one is the  $\boldsymbol{\mu}$ -isotropic limit ( $\boldsymbol{\mu}_{\perp} = \boldsymbol{\mu}_{\parallel} = \boldsymbol{\mu}$ ), which can be readily obtained from (A7) or (A9), resulting

$$\mathcal{W}_{\alpha, \beta}^{(\eta, \zeta, \boldsymbol{\mu})} = U\left(\alpha + \beta + \frac{3}{2}, \alpha + \beta + \frac{5}{2} - \zeta, \eta \boldsymbol{\mu}\right) = (\eta \boldsymbol{\mu})^{\zeta-\alpha-\beta-3/2} U\left(\zeta, \zeta - \alpha - \beta - \frac{1}{2}, \eta \boldsymbol{\mu}\right). \quad (\text{A10})$$

Another important case is the limit  $\mu_{\perp,\parallel} \rightarrow 0$ , in which case  $\mathcal{W}_{\alpha,\beta}^{(\eta,\zeta,\boldsymbol{\mu})}$  reduces to the corresponding expression for the standard bi-Kappa distribution. This is accomplished by taking the adequate limit of  $U(a,b,z)$  when  $z \rightarrow 0$  that will introduce the constraint on the lower value of  $\kappa$  imposed by the evaluation of a given moment of the VDF. Following the procedure outlined in Refs. 30 or 28, expression (A7) provides the limiting form

$$\mathcal{W}_{\alpha,\beta}^{(\eta,\zeta,0)} = \frac{\Gamma(\zeta - \alpha - \beta - 3/2)}{\Gamma(\zeta)} \left( \zeta > \frac{3}{2} + \alpha + \beta \right). \quad (\text{A11})$$

## 2. Case $z \neq 0$

Returning to (A1), we will only need the particular cases  $p_1 = -1, 0$ , for which we will obtain closed-form expression by first changing the integration variable with  $\beta = \eta\mu_{\perp}t$  and then comparing with (A4). Accordingly, we obtain

$$I_{\beta}^{(0,p_2)}(\mu_{\parallel}, \mu_{\perp}, z) = \Gamma(\zeta) \frac{(\eta\mu_{\perp})^{\zeta}}{\mu_{\perp}^{p_2}} U\left(\zeta, \zeta + 1 - p_2, \eta\mu_{\perp} \left(1 + \frac{z^2}{\eta}\right)\right) \quad (\text{A12a})$$

$$I_{\beta}^{(-1,p_2)}(\mu_{\parallel}, \mu_{\perp}, z) = \Gamma(\zeta) \frac{(\eta\mu_{\perp})^{\zeta}}{\mu_{\perp}^{p_2-1}} \left[ U\left(\zeta, \zeta + 2 - p_2, \eta\mu_{\perp} \left(1 + \frac{z^2}{\eta}\right)\right) - \mathcal{A}\boldsymbol{\mu} U\left(\zeta, \zeta + 1 - p_2, \eta\mu_{\perp} \left(1 + \frac{z^2}{\eta}\right)\right) \right]. \quad (\text{A12b})$$

## Appendix B: Susceptibility tensors for drifting bi-Maxwellian and bi-kappa populations

The specific analytical expressions of the susceptibility tensor components (6a-c) for the dbM VDF given by (3) can be found in several textbooks of kinetic theory of plasmas (see, e.g., Ref. 39) and is given by

$$\chi_1^{\text{dbM}} = \frac{1}{2} \frac{\omega_{pa}^2}{\omega^2} \sum_{s=\pm 1} \left[ \zeta_0 Z(\zeta_s) + \frac{1}{2} A_{\boldsymbol{\theta}} Z'(\zeta_s) \right] \quad (\text{B1a})$$

$$\chi_2^{\text{dbM}} = \frac{i}{2} \frac{\omega_{pa}^2}{\omega^2} \sum_{s=\pm 1} s \left[ \zeta_0 Z(\zeta_s) + \frac{1}{2} A_{\boldsymbol{\theta}} Z'(\zeta_s) \right] \quad (\text{B1b})$$

$$\chi_3^{\text{dbM}} = -\frac{\omega_{pa}^2}{\omega^2} \zeta_0^2 Z'(\zeta_0), \quad (\text{B1c})$$

where

$$Z(\zeta) = \frac{1}{\sqrt{\pi}} \int_{-\infty}^{\infty} \frac{e^{-y^2} dy}{y - \zeta} \quad (\Im \zeta > 0)$$

is the Fried & Conte function<sup>45</sup> and  $Z'(\zeta)$  its derivative.

Here, the parameters are

$$\zeta_n = \xi_n - \frac{U_{\parallel}}{\theta_{\parallel}}, \quad \xi_n = \frac{\omega - n\Omega}{k_{\parallel} \theta_{\parallel}}, \quad A_{\boldsymbol{\theta}} = 1 - \frac{T_{M,\perp}}{T_{M,\parallel}} = 1 - \frac{\theta_{\perp}^2}{\theta_{\parallel}^2},$$

where  $T_{M,\perp(\parallel)}$  is the perpendicular (parallel) temperature and  $\theta_{\perp(\parallel)}$  are the corresponding components of the thermal velocity.

The susceptibility tensor for a drifting standard Kappa distribution can be obtained as a special case of the general expressions derived in Refs. 35 and 46. The drifting standard

bi-Kappa distribution function (dbSKD) adopted here is

$$f_{\text{dbSKD}}(v_{\parallel}, v_{\perp}) = \frac{g(\kappa)}{\pi^{3/2} \theta_{\parallel} \theta_{\perp}^2} \left[ 1 + \frac{(v_{\parallel} - U_{\parallel})^2}{\kappa \theta_{\parallel}^2} + \frac{v_{\perp}^2}{\kappa \theta_{\perp}^2} \right]^{-(\kappa+1)}, \quad (\text{B2})$$

which is valid for  $\kappa > 1/2$  and where  $g(\kappa) = \Gamma(\kappa) / \kappa^{1/2} \Gamma(\kappa - 1/2)$ .

For the distribution (B2), the susceptibility tensor is

$$\chi_1^{(\text{dbSKD})} = \frac{1}{2} \frac{\omega_{pa}^2}{\omega^2} \sum_{s=\pm 1} \left[ \zeta_0 Z_{\kappa}^{(0)}(\zeta_s) + \frac{1}{2} A_{\boldsymbol{\theta}} Z_{\kappa}^{(-1)'}(\zeta_s) \right] \quad (\text{B3a})$$

$$\chi_2^{(\text{dbSKD})} = \frac{i}{2} \frac{\omega_{pa}^2}{\omega^2} \sum_{s=\pm 1} s \left[ \zeta_0 Z_{\kappa}^{(0)}(\zeta_s) + \frac{1}{2} A_{\boldsymbol{\theta}} Z_{\kappa}^{(-1)'}(\zeta_s) \right] \quad (\text{B3b})$$

$$\chi_3^{(\text{dbSKD})} = -\frac{\omega_{pa}^2}{k_{\parallel}^2 \theta_{\parallel}^2} Z_{\kappa}^{(0)'}(\zeta_0). \quad (\text{B3c})$$

In (B3a-c), the tensor components are written in terms of the (standard) kappa dispersion function

$$Z_{\kappa}^{(\beta)}(\xi) = \frac{\kappa^{-\beta-1/2} \Gamma(\kappa + \beta)}{\pi^{1/2} \Gamma(\kappa - 1/2)} \int_{-\infty}^{\infty} ds \frac{(1 + s^2/\kappa)^{-(\kappa+\beta)}}{s - \xi},$$

which is valid for  $\kappa + \beta > 0$ . This function and its derivative can be evaluated from the representation

$$Z_{\kappa}^{(\beta)}(\xi) = i \frac{\kappa^{-\beta-1/2} \Gamma(\kappa + \beta + 1/2)}{(\kappa + \beta) \Gamma(\kappa - 1/2)} \times F \left[ \begin{matrix} 1, 2(\kappa + \beta) \\ \kappa + \beta + 1 \end{matrix}; \frac{1}{2} \left( 1 + \frac{i\xi}{\kappa^{1/2}} \right) \right],$$

where  $F(\dots)$  is the Gauss hypergeometric function.<sup>47</sup>

The function  $Z_{\kappa}^{(\beta)}(\xi)$  and its derivative are also related by

$$Z_{\kappa}^{(\beta)'}(\xi) = -2 \left[ \frac{\Gamma(\kappa + \beta + 1/2)}{\kappa^{\beta+1} \Gamma(\kappa - 1/2)} + \xi Z_{\kappa}^{(\beta+1)}(\xi) \right].$$

- <sup>1</sup>v. Štverák, P. Trávníček, M. Maksimovic, E. Marsch, A. N. Fazakerley, and E. E. Scime, *Journal of Geophysical Research: Space Physics* **113**, A03103 (2008), <https://agupubs.onlinelibrary.wiley.com/doi/pdf/10.1029/2007JA012733>.
- <sup>2</sup>L. B. Wilson, III, L.-J. Chen, S. Wang, S. J. Schwartz, D. L. Turner, M. L. Stevens, J. C. Kasper, A. Osmane, D. Caprioli, S. D. Bale, M. P. Pulupa, C. S. Salem, and K. A. Goodrich, *Astrophysical Journal Supplement Series* **243**, 8 (2019a).
- <sup>3</sup>L. B. Wilson, L.-J. Chen, S. Wang, S. J. Schwartz, D. L. Turner, M. L. Stevens, J. C. Kasper, A. Osmane, D. Caprioli, S. D. Bale, M. P. Pulupa, C. S. Salem, and K. A. Goodrich, *The Astrophysical Journal Supplement Series* **245**, 24 (2019b).
- <sup>4</sup>J. S. Halekas, P. L. Whittlesey, D. E. Larson, D. McGinnis, S. D. Bale, M. Berthomier, A. W. Case, B. D. G. Chandran, J. C. Kasper, K. G. Klein, K. E. Korreck, R. Livi, R. J. MacDowall, M. Maksimovic, D. M. Malaspina, L. Matteini, M. P. Pulupa, and M. L. Stevens, *Astronomy & Astrophysics* **650**, A15 (2021).
- <sup>5</sup>J. B. Abraham, C. J. Owen, D. Verscharen, M. Bakrania, D. Stansby, R. T. Wicks, G. Nicolaou, P. L. Whittlesey, J. A. Agudelo Rueda, S.-Y. Jeong, and L. Berčič, *Astrophysical Journal* **931**, 118 (2022).
- <sup>6</sup>L. Berčič, D. Verscharen, C. J. Owen, L. Colombari, M. Kretzschmar, T. Chust, M. Maksimovic, D. O. Kataria, C. Anekallu, E. Behar, M. Berthomier, R. Bruno, V. Fortunato, C. W. Kelly, Y. V. Khotyaintsev, G. R. Lewis, S. Livi, P. Louarn, G. Mele, G. Nicolaou, G. Watson, and R. T. Wicks, *Astronomy & Astrophysics* **656**, A31 (2021).
- <sup>7</sup>J. T. Coburn, D. Verscharen, C. J. Owen, M. Maksimovic, T. S. Horbury, C. H. K. Chen, F. Guo, X. Fu, J. Liu, J. B. Abraham, G. Nicolaou, M. E. Innocenti, A. Micera, and V. K. Jagarlamudi, *Astrophysical Journal* **964**, 100 (2024).
- <sup>8</sup>D. Verscharen, B. D. G. Chandran, E. Boella, J. Halekas, M. E. Innocenti, V. K. Jagarlamudi, A. Micera, V. Pierrard, Š. Štverák, I. Y. Vasko, M. Velli, and P. L. Whittlesey, *Frontiers in Astronomy and Space Sciences* **9**, 951628 (2022).
- <sup>9</sup>M. Lazar, R. A. López, S. M. Shaaban, S. Poedts, P. H. Yoon, and H. Fichtner, *Frontiers in Astronomy and Space Sciences* **8**, 249 (2022).
- <sup>10</sup>S. M. Shaaban, R. A. López, M. Lazar, and S. Poedts, *Astronomy & Astrophysics* **691**, A86 (2024).
- <sup>11</sup>D. Verscharen, B. D. G. Chandran, S.-Y. Jeong, C. S. Salem, M. P. Pulupa, and S. D. Bale, *Astrophysical Journal* **886**, 136 (2019).
- <sup>12</sup>S. P. Gary, *Theory of Space Plasma Microinstabilities*, Cambridge Atmospheric and Space Science Series (Cambridge University Press, Cambridge, 2005) 181 + xii pp.
- <sup>13</sup>P. H. Yoon, *Reviews of Modern Plasma Physics* **1**, 4 (2017).
- <sup>14</sup>S. M. Shaaban, M. Lazar, R. A. López, P. H. Yoon, and S. Poedts, in *Kappa Distributions; From Observational Evidences via Controversial Predictions to a Consistent Theory of Nonequilibrium Plasmas*, Astrophysics and Space Science Library, Vol. 464, edited by M. Lazar and H. Fichtner (2021) pp. 185–218.
- <sup>15</sup>R. A. López, P. S. Moya, S. M. Shaaban, M. Lazar, P. H. Yoon, and S. Poedts, in *Kappa Distributions; From Observational Evidences via Controversial Predictions to a Consistent Theory of Nonequilibrium Plasmas*, Astrophysics and Space Science Library, Vol. 464, edited by M. Lazar and H. Fichtner (2021) pp. 163–184.
- <sup>16</sup>S. Olbert, *Physics of the Magnetosphere* **10**, 641 (1968).
- <sup>17</sup>V. M. Vasyliunas, *Journal of Geophysical Research* (1896-1977) **73**, 2839 (1968), <https://agupubs.onlinelibrary.wiley.com/doi/pdf/10.1029/JA073i009p02839>.
- <sup>18</sup>K. Scherer, H. Fichtner, and M. Lazar, *EPL (Europhysics Letters)* **120**, 50002 (2017).
- <sup>19</sup>D. Summers and R. M. Thorne, *Physics of Fluids B: Plasma Physics* **3**, 1835 (1991), ....
- <sup>20</sup>K. Scherer, E. Husidic, M. Lazar, and H. Fichtner, *Mont. Not. R. Astron. Soc.* **497**, 1738–1756 (2020).
- <sup>21</sup>K. Scherer, E. Husidic, M. Lazar, and H. Fichtner, *Astronomy & Astrophysics* **663**, A67 (2022).
- <sup>22</sup>M. Lazar and H. Fichtner, in *Kappa Distributions; From Observational Evidences via Controversial Predictions to a Consistent Theory of Nonequilibrium Plasmas*, Astrophysics and Space Science Library, Vol. 464, edited by M. Lazar and H. Fichtner (2021) pp. 107–123.
- <sup>23</sup>E. Husidic, M. Lazar, H. Fichtner, K. Scherer, and S. Poedts, *Astronomy & Astrophysics* **654**, A99 (2021).
- <sup>24</sup>K. Scherer, H. Fichtner, H. J. Fahr, and M. Lazar, *Astrophysical Journal* **881**, 93 (2019).
- <sup>25</sup>E. Husidic, K. Scherer, M. Lazar, H. Fichtner, and S. Poedts, *Astrophysical Journal* **927**, 159 (2022).
- <sup>26</sup>L.-N. Hau, C.-K. Chang, and M. Lazar, *Astrophysical Journal* **956**, 144 (2023).
- <sup>27</sup>A. A. El-Tantawy, W. F. El-Taibany, S. K. El-Labany, and A. M. Abdelghany, *Physics of Plasmas* **31**, 042111 (2024).
- <sup>28</sup>R. Gaelzer and L. F. Ziebell, *Physics of Plasmas* **32**, 033706 (2025).
- <sup>29</sup>E. Husidic, M. Lazar, H. Fichtner, K. Scherer, and P. Astfalk, *Physics of Plasmas* **27**, 042110 (2020).
- <sup>30</sup>R. Gaelzer, H. Fichtner, and K. Scherer, *Phys. Plasmas* **31**, 072112 (2024).
- <sup>31</sup>L.-N. Hau, C.-S. Jao, and C.-K. Chang, *Physics of Plasmas* **31**, 032113 (2024).
- <sup>32</sup>D. L. Schröder, H. Fichtner, M. Lazar, D. Verscharen, and K. G. Klein, *Phys. Plasmas* **32**, 032109 (2025).
- <sup>33</sup>D. L. Schröder, M. Lazar, R. A. López, and H. Fichtner, *Astrophys. J.* **987**, 110 (2025).
- <sup>34</sup>R. Gaelzer and L. F. Ziebell, *Phys. Plasmas* **23**, 022110 (2016).
- <sup>35</sup>R. Gaelzer, L. F. Ziebell, and A. R. Meneses, *Phys. Plasmas* **23**, 062108 (2016).
- <sup>36</sup>D. Verscharen, K. G. Klein, B. D. G. Chandran, M. L. Stevens, C. S. Salem, and S. D. Bale, *Journal of Plasma Physics* **84** (2018), [10.1017/s0022377818000739](https://doi.org/10.1017/s0022377818000739).
- <sup>37</sup>R. López, S. Shaaban, and M. Lazar, *Journal of Plasma Physics* **87**, 905870310 (2021).
- <sup>38</sup>M. Lazar, S. Poedts, and H. Fichtner, *Astronomy & Astrophysics* **582**, A124 (2015).
- <sup>39</sup>M. Brambilla, *Kinetic Theory of Plasma Waves: Homogeneous Plasmas*, International series of monographs on physics (Clarendon Press, New York, 1998) 644 + x pp.
- <sup>40</sup>J. S. Halekas, P. Whittlesey, D. E. Larson, M. Maksimovic, R. Livi, M. Berthomier, J. C. Kasper, A. W. Case, M. L. Stevens, S. D. Bale, R. J. MacDowall, and M. P. Pulupa, *Astrophys. J.* **936**, 53 (2022).
- <sup>41</sup>D. L. Schröder, M. Lazar, H. Fichtner, R. A. López, and S. Poedts, *Astronomy & Astrophysics* **709**, A3 (2026).
- <sup>42</sup>S. M. Shaaban, M. Lazar, and S. Poedts, *Mont. Not. R. Astron. Soc.* **480**, 310–319 (2018).
- <sup>43</sup>S. M. Shaaban, M. Lazar, P. H. Yoon, and S. Poedts, *Phys. Plasmas* **25**, 082105 (2018).
- <sup>44</sup>A. B. O. Daalhuis, in<sup>48</sup>, Chap. 13, p. 321–349.
- <sup>45</sup>B. D. Fried and S. D. Conte, *The plasma dispersion function: the Hilbert transform of the Gaussian* (Academic Press, New York, 1961) 419 pp.
- <sup>46</sup>A. R. Meneses, R. Gaelzer, and L. F. Ziebell, *Phys. Plasmas* **25**, 112901 (2018).
- <sup>47</sup>A. B. O. Daalhuis, in<sup>48</sup>, Chap. 15, p. 383–401.
- <sup>48</sup>F. W. J. Olver, D. W. Lozier, R. F. Boisvert, and C. W. Clark, eds., *NIST Handbook of Mathematical Functions* (Cambridge, New York, 2010).